Direct numerical simulation of electrokinetic transport phenomena: variational multi-scale stabilization and octree-based mesh refinement

Sungu Kim^{a,b,*}, Kumar Saurabh^{a,*}, Makrand A. Khanwale^{c,*}, Ali Mani^c, Robbyn K. Anand^b, Baskar Ganapathysubramanian^{a,**}

^{a}*Department of Mechanical Engineering, Iowa State University, Iowa, USA 50011*
^{b}*Department of Chemistry, Iowa State University, Iowa, USA 50011*
^{c}*Center for Turbulence Research, Stanford University, Stanford, California, USA 94305*

Abstract

Finite element modeling of charged species transport has enabled the analysis, design, and optimization of a diverse array of electrochemical and electrokinetic devices. These systems are represented by the Poisson-Nernst-Planck (PNP) equations coupled with the Navier-Stokes (NS) equation. Direct numerical simulation (DNS) to accurately capture the spatio-temporal variation of ion concentration and current flux remains challenging due to the (a) small critical dimension of the electric double layer (EDL), (b) stiff coupling, large advective effects, and steep gradients close to boundaries, and (c) complex geometries exhibited by electrochemical devices.

In the current study, we address these challenges by presenting a direct numerical simulation framework that incorporates: (a) a variational multiscale (VMS) treatment, (b) a block-iterative strategy in conjunction with semi-implicit (for NS) and implicit (for PNP) time integrators, and (c) octree based adaptive mesh refinement. The VMS formulation provides numerical stabilization critical for capturing the electro-convective instabilities often observed in engineered devices. The block-iterative strategy decouples the difficulty of non-linear coupling between the NS and PNP equations and allows using tailored numerical schemes separately for NS and PNP equations. The carefully designed second-order, hybrid implicit methods circumvent the harsh timestep requirements of explicit time steppers, thus enabling simulations over longer time horizons. Finally, the octree-based meshing allows efficient and targeted spatial resolution of the EDL. These features are incorporated into a massively parallel computational framework, enabling the simulation of realistic engineering electrochemical devices. The numerical framework is illustrated using several challenging canonical examples.

Keywords: electrokinetics, electrohydrodynamics, Navier-Stokes Poisson Nernst-Planck, octrees, variational multiscale approach

1. Introduction

A diverse set of energy conversion, energy storage, manufacturing, and healthcare processes are characterized by the transport and interaction of charged species in aqueous environments. These interactions span multiple time and length scales, often involving complex geometries [1–6]. Examples of such processes include electrolysis for hydrogen production, electrodialysis for water

---

*These three authors contributed equally
**Corresponding author
Email address: `baskarg@iastate.edu` (Baskar Ganapathysubramanian)

desalination, gas diffusion electrodes for chemical conversion, carbon capture, as well as several other processes that have a direct impact on sustainability and climate resilience [7–12].

Quantitative analyses of such processes are performed using continuum mechanics-derived partial differential equations (PDEs), specifically the Navier-Stokes (NS) and the Poisson-Nernst-Plank (PNP) equations. Often, detailed, high-fidelity simulations — i.e., direct numerical simulations — are critical for comprehensive understanding and design of electrokinetic systems. However, the complexities arising from the tight coupling of multiscale and multiphysics phenomena in these processes make simulating these systems very challenging. A comprehensive simulation framework can significantly accelerate the exploration and understanding of complex electrochemical processes and enable the design and optimization of societally relevant applications like more efficient water electrolysis and cheaper and lightweight dialysis machines.

One can broadly identify three challenges to performing direct numerical simulations of NS-PNP equations in complex geometries: First, electrokinetic systems involve coupled mass transport, fluid flow, and electrodynamics. This stiff coupling between the NS and PNP equation is responsible for producing a variety of very interesting phenomena [7–15]. For instance, even in systems with small hydrodynamic velocities, i.e., low Reynolds (Re) numbers, a strong applied electric field triggers strongly non-linear and multi-scale electrokinetic instabilities [16]. This calls for numerical methods that can robustly and efficiently capture stiff coupling. Second, such systems often exhibit thin regions with a high electric field and high gradients in ion concentration, usually near the boundary. Accurately resolving these near-boundary gradients is essential, as they determine not only the bulk behavior but also impact the boundary fluxes, which are often the quantities of most interest from an experimental point of view [17–20]. The challenge of accurately resolving these regions is further exacerbated by the complex geometries exhibited by various electrochemical devices (packed beds, dendritic surfaces). This calls for approaches that are endowed with the ability to spatially resolve complex geometries in a scalable fashion. Third, simulating practical systems of engineering interest requires performing simulations across a long time horizon. This calls for time discretizations that are higher order and have good stabilizing properties, thus offering the ability to successfully capture long time horizon simulations affordably [21].

Resolving these challenges requires careful design of spatial stabilization and temporal discretization as well as appropriate strategies of (de)coupled solution of the equations and adaptive mesh refinement. To resolve those challenges, Druzgalski et al. [16] performed pioneering direct numerical simulations of electroconvective instabilities. They used a non-uniform mesh in the wall-normal direction to resolve the EDLs for small Debye lengths and a semi-implicit time scheme. The framework was then pushed for more complicated geometries and patterned surfaces in [22, 23]. One of the main challenges in simulating these systems is that if one resolves the thin EDLs with a fine mesh resolution, one often requires very small timesteps for stability reasons. The problem of resolving thin EDLs is exacerbated when the problem length scale is larger, i.e., small non-dimensional Debye lengths, requiring even finer meshes and even smaller timesteps. Additionally, instabilities generated under high electric fields require subgrid-scale modeling as the mesh is coarsened away from the fine resolution near the boundary.

There have been computational studies using commercial software to analyze the non-linear behavior of electrokinetics [24–26]. It is important to note that most commercial software is unsuitable for such electrochemical systems, either because the numerical methods are not designed for these phenomena or they are not scalable enough to accurately resolve the spatial and temporal scales required. For example, Karatay et al. [27] showed that with a carefully designed numerical method, their code was 20× faster than the commercial alternative (COMSOL in this case) on a single processor. This advantage shot up to about 160× speed up when both the codes were deployed in parallel but on a single node. Therefore, careful design of numerical methods and efficient par-

allel implementation are essential for affordable high-fidelity simulations of electrochemical sys-
tems. While there has been some progress in developing flexible frameworks [28, 29], numerical
challenges involved in solving the PNP equations still remain.

In this work, we seek to resolve all three challenges detailed above for the direct numerical sim-
ulation of electrokinetic phenomena. We build upon our previous work on a finite elements based
framework for solving the NS and PNP equations [30]. Finite element approaches have been suc-
cessfully applied for high-resolution simulations of NS (See [31] for an overview) and PNP [32–
40] equations. They are well suited for the NS-PNP system of equations due to (a) the use of a
variational formulation that allows the weakening of derivatives, (b) the natural incorporation of
heterogeneous and mixed boundary conditions often seen in these systems, and (c) ability to con-
struct rigorous *a posteriori* error estimates for mesh adaptivity that enable substantial computational
gains away from the EDLs.

The main contributions of this paper are as follows:

1. We decouple the solution procedure of NS and PNP equations in a block-solve strategy. The
   PNP equations are solved using a fully implicit Newton method-based non-linear solver, en-
   suring the choice of large time steps even for cases with very fine mesh resolution used for thin
   EDLs. On the other hand, the Navier-Stokes equations are discretized using a semi-implicit
   linear discretization which also ensures stability for larger time steps. In conjunction with
   this strategy, we utilize a second-order time discretization for both NS and PNP to ensure ac-
   curacy across long time horizons. This block-iterative strategy, in conjunction with carefully
   chosen preconditioners, allows robust and efficient DNS computations.

2. We use a variational multi-scale (VMS) based stabilization for the pressure that allows for a
   pressure-coupled solver in conjunction with continuous Galerkin finite elements. Addition-
   ally, the VMS method provides sub-grid scale modeling for fine-scale velocities and ion con-
   centrations not resolved by the grid size. This allows us to use adaptive mesh discretization
   without compromising the accuracy of the field variables.

3. We use a massively parallel octree-based meshing framework to resolve the thin EDLs for
   small Debye lengths, as well as mesh complex geometries in 3D. We use Dendro-KT, a highly
   scalable parallel octree library, to generate, manage and traverse adaptive octree-based meshes
   in distributed memory. Octrees are widely used in computational sciences [41–48], due to its
   conceptual simplicity and ability to scale across a large number of processors.

4. We illustrate the framework with a series of increasingly difficult simulations exhibiting electro-
   convective instabilities and complex geometries.

The rest of the paper is structured as follows: Section 2 details the equations in non-dimensional
form. Section 3 lays out the spatial and temporal discretization and associated properties. Section
4 describes the implementation and algorithmic details of the framework. Section 5 reports on
the numerical results, starting from convergence tests using manufactured solutions to a full 3D
simulation of a bio-diagnostic device. We conclude in Section 6.

2. Governing equations

2.1. Dimensional form:

Consider a bounded domain $\Omega \subset \mathbb{R}^d$ (for $d = 2, 3$) and the time interval $[0, T]$. The domain
contains a fluid (usually aqueous) with N ionic species, and we seek to model the behavior of
the N species concentration under the imposition of electric fields. The concentration distribution
of the N species is represented using Nernst-Plank transport equations, along with the Poisson
equation for the electric potential, together making up the Poisson-Nernst-Plank (PNP) equations.

The pressure and fluid velocity are represented using the Navier Stokes (NS) equations. There is a two-way coupling between the species concentration and the underlying fluid motion, given by an advection term in the PNP equation and an electrohydrodynamic term in the NS equation.

We consider $N > 1$ number of charged species with subscript s indicating the species index. The species flux, $j_i^{s,*}$, which is driven by diffusion, migration, and convection is written as:

$$j_i^{s,*} = -D^s \frac{\partial c^{s,*}}{\partial x_i^*} - D^s \frac{z^s F}{RT} c^{s,*} \frac{\partial \phi^{s,*}}{\partial x_i^*} + v_i^* c^{s,*} \qquad \text{for } s^{th} \text{ species,} \tag{1}$$

D^s is diffusivity of sth species, $c^{s,*}$ is concentration of sth species, z^s is valance of sth species, F is Faraday constant 96,485.33 C/mol, R is gas constant 8.314 J/mol K, T is temperature, ϕ^* is electric potential, and v_i^* is fluid velocity.

Remark 1. *Note that we use Einstein notation throughout this work; in this notation, v_i represents the ith component of the vector $\mathbf{v}$, and any repeated index is implicitly summed over. Superscript s is the species index. To avoid confusion powers of the terms are represented by writing the power outside the braces. For example square of sth species of concentration is written as $(c^{s,*})^2$. For non-dimensional quantities, $*$ in the superscript will be dropped.*

The time variation of concentration can be obtained by taking the divergence of species flux,

$$\frac{\partial c^{s,*}}{\partial t^*} = -\frac{\partial j_i^{s,*}}{\partial x_i^*}, \qquad \text{for the } s^{th} \text{ species.} \tag{2}$$

Combining eqs. (1) and (2) and assuming that the fluid is incompressible $\frac{\partial v_i^*}{\partial x_i^*} = 0$ produces the Nernst-Planck equation,

$$\frac{\partial c^{s,*}}{\partial t^*} + v_i^* \frac{\partial c^{s,*}}{\partial x_i^*} = \frac{\partial}{\partial x_i^*} \left(D^s \frac{\partial c^{s,*}}{\partial x_i^*} + D^s \frac{z^s F}{RT} c^{s,*} \frac{\partial \phi^{s,*}}{\partial x_i^*} \right). \tag{3}$$

The second term on the left-hand side of Eqn. 3 represents the advective transport of species, which is the coupling between the species concentration and the flow field. The first term on the right-hand side of Eqn. 3 represents the diffusion of species, while the second term represents the electric migration of species.

The electric potential, ϕ^* in the domain, depends on the concentration distribution of the N species and the imposed electric field. The potential is the solution to the Poisson equation [49]

$$\frac{\partial}{\partial x_i^*} \left(-\varepsilon \frac{\partial \phi^*}{\partial x_i^*} \right) = \rho_e^*. \tag{4}$$

ε is the electric permittivity of fluid, and ρ_e is charge density. Charge density can be expressed with species concentration.

$$\rho_e^* = F \sum c^{s,*} z^s \tag{5}$$

Then, equation (4) becomes (assuming that the permittivity, ε, is constant)

$$-\varepsilon \frac{\partial}{\partial x_i^*} \left(\frac{\partial \phi^*}{\partial x_i^*} \right) = F \sum c^{s,*} z^s. \tag{6}$$

4

Finally, the Navier-Stokes equation is written as,

$$\rho \frac{\partial v_i^*}{\partial t^*} + \rho \frac{\partial \left(v_j^* v_i^* \right)}{\partial x_j^*} + \frac{\partial p^*}{\partial x_i^*} - \eta \frac{\partial}{\partial x_j^*} \left(\frac{\partial v_i^*}{\partial x_j^*} \right) - \rho_e^* E_i^* = 0 \tag{7}$$

ρ is the density of the fluid, p is pressure, η is dynamic viscosity, and E_i is i^{th} component of the electric field. The last term in the above equation is the body force due to the electric field. This is the coupling between the NS and the PNP. Using the relationship between electric potential and electric field,

$$-\frac{\partial \phi^*}{\partial x_i^*} = E_i^*, \tag{8}$$

and from the expression of charge density (equation (5)), equation (7) can be written as

$$\rho \frac{\partial v_i^*}{\partial t^*} + \rho \frac{\partial \left(v_j^* v_i^* \right)}{\partial x_j^*} + \frac{\partial p^*}{\partial x_i^*} - \eta \frac{\partial}{\partial x_j^*} \left(\frac{\partial v_i^*}{\partial x_j^*} \right) + F \sum c^{s,*} z^s \frac{\partial \phi^*}{\partial x_i^*} = 0. \tag{9}$$

Remark 2. *Note that some papers in the literature use elementary charge e and Boltzmann constant k_B instead of Faraday constant F and gas constant R [50]. The choice of these parameters is simply dependent on how to define concentration. Here, we choose the Faraday constant, F, and gas constant R since molarity M was used for concentration.*

We write all the governing equations together as,

$$\text{Momentum Eqns:} \quad \rho \frac{\partial v_i^*}{\partial t^*} + \rho \frac{\partial \left(v_j^* v_i^* \right)}{\partial x_j^*} + \frac{\partial p^*}{\partial x_i^*} - \eta \frac{\partial}{\partial x_j^*} \left(\frac{\partial v_i^*}{\partial x_j^*} \right) + F \left(\sum c^{s,*} z^s \right) \frac{\partial \phi^*}{\partial x_i^*} = 0, \tag{10}$$

$$\text{Poisson:} \quad -\varepsilon \frac{\partial}{\partial x_i^*} \left(\frac{\partial \phi^*}{\partial x_i^*} \right) = F \sum c^{s,*} z^s, \tag{11}$$

$$\text{Nernst-Planck:} \quad \frac{\partial c^{s,*}}{\partial t^*} + v_i^* \frac{\partial c^{s,*}}{\partial x_i^*} = \frac{\partial}{\partial x_i^*} \left(D^s \frac{\partial c^{s,*}}{\partial x_i^*} + D^s \frac{z^s F}{RT} c^{s,*} \frac{\partial \phi^*}{\partial x_i^*} \right). \tag{12}$$

Table 1 shows all the dimensional parameters involved.

Parameters	Units	Value/Formula
Species diffusivity, D^s	m^2/s	
Species valence, z^s		
Faraday constant, F	C/mol	$96,485.33\ C/mol$
Gas constant, R	$J/K \cdot mol$	$8.314\ J/K \cdot mol$
Temperature, T	K	
Vacuum permittivity, ε_0	$F/m,\ C/V \cdot m,\ N/V^2$	$8.854 \times 10^{-12} F/m$
Relative permittivity, ε_r		
Permittivity, ε	$F/m,\ C/V \cdot m,\ N/V^2$	$\varepsilon = \varepsilon_r \varepsilon_0$
Charge density, ρ_e	C	
Density, ρ	kg/m^3	
Viscosity, η	$Pa \cdot s,\ cP$	$8.90 \times 10^{-4} P \cdot s$ for water at $25\,°C$
Ionic strength of bulk, I_b	$M,\ mol/m^3$	$I_b = \frac{1}{2}\Sigma z_i^2 c_i$
Thermal voltage, V_T	V	$V_T = RT/F$

Table 1: Dimensional parameters in the governing equations.

2.2. Non-dimensional form:

Each variable is scaled with its associated reference quantity to define its non-dimensional counterpart.

$$x_i = \frac{x_i^*}{L_{ch}}, \quad t = \frac{t^*}{t_{ch}}, \quad v_i = \frac{v_i^*}{U_{ch}}, \quad p = \frac{p^*}{p_{ch}}, \quad c_i = \frac{c_i^*}{c_{ch}}, \quad \phi = \frac{\phi^*}{\phi_{ch}}. \tag{13}$$

And for the derivative terms,

$$\frac{\partial}{\partial x_i} = L_{ch}\frac{\partial}{\partial x_i^*}, \quad \frac{\partial}{\partial x_i}\left(\frac{\partial}{\partial x_i}\right) = L_{ch}^2 \frac{\partial}{\partial x_i^*}\left(\frac{\partial}{\partial x_i^*}\right) \tag{14}$$

To non-dimensionalize the governing equations, it is important to select appropriate reference quantities in eq. (13). We typically consider internal flows (like in microfluidic channels), and the reference length L_{ch} is the channel width L for 2-dimensional problems or the hydraulic diameter D_h for 3-dimensional problems. The reference concentration and reference potential are selected as follows:

$$c_{ch} = I_b = \frac{1}{2}\sum (z^s)^2 c^s \quad \text{and} \quad \phi_{ch} = V_T = \frac{RT}{F} \tag{15}$$

I_b is the ionic strength of bulk, and V_T is the thermal voltage. The rest of the variables have multiple options to choose from for the reference quantity. We choose the following reference quantities: The characteristic velocity U_{ch} is given by D/L, characteristic time t_{ch} given by L^2/D, and characteristic pressure given by $\eta D/L^2$. Here, D is the mean species diffusivity, and η is the dynamic viscosity of the fluid medium.

With these characteristic quantities, the non-dimensional equations are given as follows,

$$\text{Momentum Eqns:} \quad \frac{1}{Sc}\left(\frac{\partial v_i}{\partial t} + \frac{\partial (v_j v_i)}{\partial x_j}\right) + \frac{\partial p}{\partial x_i} - \frac{\partial^2 v_i}{\partial x_j^2} + \frac{\kappa}{2\Lambda^2}\left(\sum c^s z^s\right)\frac{\partial \phi}{\partial x_i} = 0, \tag{16}$$

$$\text{Solenoidality:} \quad \frac{\partial v_i}{\partial x_i} = 0, \tag{17}$$

6

$$\text{Poisson:} \quad -2\Lambda \frac{\partial^2 \phi}{\partial x_i^2} = \sum c^s z^s, \tag{18}$$

$$\text{Nernst-Planck:} \quad \frac{\partial c^s}{\partial t} + v_i \frac{\partial c^s}{\partial x_i} = \frac{\partial}{\partial x_i} \left(\frac{\partial c^s}{\partial x_i} + z^s c^s \frac{\partial \phi}{\partial x_i} \right). \tag{19}$$

Where the Schmidt number, $Sc = \frac{\eta}{\rho D}$, the electrohydrodynamic (EHD) constant, $\kappa = \frac{\varepsilon}{\eta D^2} \left(\frac{RT}{F} \right)^2$, and non-dimensionalized Debye length, $\Lambda = \lambda_D / L_{ch}$, where λ_D is the Debye length, $\lambda_D = \sqrt{\frac{1}{2} \frac{\varepsilon RT}{F^2 I_b}}$.

3. Numerical method and its properties

We use a second order backward difference formula (BDF) scheme as a time-stepping strategy for eqs. (16) to (19). We solve momentum equations and Poisson Nernst-Planck (PNP) equations in two separate blocks.

Let δt be a time-step; let $t^k := k\delta t$; Let $n + 1$ be the current time-point, and n be the previous time-point. We define an intermediate velocity at time $n + 1$ as follows:

$$\widetilde{\mathbf{v}}^{k+1} := 2\mathbf{v}^k - \mathbf{v}^{k-1}, \tag{20}$$

We define our time-discretized weak form of the Navier-Stokes-Poisson-Nernst-Plank (NS-PNP) equations are as follows:

7

Let $(\cdot, \cdot)$ be the standard L^2 inner product. We state the time-discrete variational problem as follows: find $\mathbf{v}^{k+1}(\mathbf{x}) \in \mathbf{H}^r(\Omega)$, $p^{k+1}(\mathbf{x})$, $\phi^{k+1}(\mathbf{x})$, $c^{s,k+1}(\mathbf{x}) \in H^r(\Omega)$ such that

Momentum Eqns:
$$\frac{1}{Sc}\left(w_i, \frac{\beta_0 v_i^{k+1} + \beta_1 v_i^k + \beta_2 v_i^{k-1}}{\delta t}\right)_\Omega + \frac{1}{Sc}\left(w_i, \widetilde{v}_j^{k+1} \frac{\partial v_i^{k+1}}{\partial x_j}\right)_\Omega$$
$$+ \left(w_i, \frac{\partial p^{k+1}}{\partial x_i}\right)_\Omega + \left(\frac{\partial w_i}{\partial x_j}, \frac{\partial v_i^{k+1}}{\partial x_j}\right)_\Omega - \left(w_i, \hat{n}_j \frac{\partial v_i^{k+1}}{\partial x_j}\right)_{\partial\Omega} \qquad (21)$$
$$+ \frac{\kappa}{2\Lambda^2}\left(\sum c^{s,k+1} z^s\right)\frac{\partial \phi^{k+1}}{\partial x_i} = 0,$$

Solenoidality:
$$\left(q, \frac{\partial v_i^{k+1}}{\partial x_i}\right)_\Omega = 0, \qquad (22)$$

Poisson:
$$2\Lambda\left(\frac{\partial q}{\partial x_i}, \frac{\partial \phi^{k+1}}{\partial x_i}\right)_\Omega - 2\Lambda\left(q, n_i \frac{\partial \phi^{k+1}}{\partial x_i}\right)_{\partial\Omega} - \left(q, \sum c^{s,k+1} z^s\right)_\Omega = 0, \quad (23)$$

Nernst-Planck:
$$\left(q, \frac{\beta_0 c^{s,k+1} + \beta_1 c^{s,k} + \beta_2 c^{s,k-1}}{\delta t}\right)_\Omega + \left(q, \widetilde{v}_i^{k+1}\frac{\partial c^{s,k+1}}{\partial x_i}\right)_\Omega$$
$$+ \left(\frac{\partial q}{\partial x_i}, \frac{\partial c^{s,k+1}}{\partial x_i} + z^s c^{s,k+1}\frac{\partial \phi^{k+1}}{\partial x_i}\right)_\Omega \qquad (24)$$
$$- \left(q, \hat{n}_i\left(\frac{\partial c^{s,k+1}}{\partial x_i} + z^s c^{s,k+1}\frac{\partial \phi^{k+1}}{\partial x_i}\right)\right)_{\partial\Omega} = 0,$$

$\forall \mathbf{w} \in \mathbf{H}^r(\Omega)$, $\forall q \in H^r(\Omega)$, given $\mathbf{v}^k$, $\mathbf{v}^{k-1} \in \mathbf{H}^r(\Omega)$, and $\phi^k, \phi^{k-1}, c^{s,k}, c^{s,k} \in H^r(\Omega)$. $\hat{\mathbf{n}}$ is the outward pointing normal to the boundary $\partial\Omega$

Remark 3. *Note that the variational forms above are for general Hilbert spaces with regularity r (order of allowed derivatives in the space). However, for the cases in this paper, we restrict ourselves to r = 1, which corresponds to bilinear basis functions.*

3.1. Spatial discretization and the variational multiscale approach

We use continuous Galerkin finite elements for spatial discretization of the time-discrete system presented in definition 1. However, imposing the d'Alembert constraint (eq. (22)) when solving $\mathbf{v}$, p together presents a challenge. An equal order polynomial approximation of velocity and pressure leads to pressure instability because of the violation of the discrete inf-sup condition (Ladyzhenskaya-Babuska-Brezzi condition, e.g., see Volker [31, page 31]). There are two ways to circumvent this issue; 1) add pressure stabilization to eq. (22), which converts the inf-sup stability restriction to a V-elliptic coercivity problem [51], thereby curbing the artificial pressure instabilities; 2) The second method is to solve a separate pressure Poisson equation using the Helmholtz Hodge decomposition of solenoidal velocity fields. For our specific problem of NS-PNP equations, we choose to use method 1. Choosing method one allows us to use the Variational multi-scale method (VMS) [52] to stabilize pressure. In addition to providing pressure stabilization, VMS also has a very useful feature. It allows us to naturally perform Large Eddy simulation type decomposition

and appropriate subgrid scale modeling [53]. The VMS enrichment for modeling fine-scale velocities, pressures and ion concentrations allows us to coarsen away from the extremely fine resolutions near the boundary, resolving the thin EDLs. Note that providing targeted resolution near the boundary for resolving EDLs is relatively simpler, however resolving emerging small-scale structures due to electrochemical instabilities for high electric fields is extremely difficult without doing adaptive meshing [1]. Therefore, the subgrid-scale modeling away from the fine resolutions of the EDLs is valuable for accurately capturing electroconvective instabilities with relatively coarser resolutions.

The VMS approach uses a direct-sum decomposition of the function spaces as follows. If $\mathbf{v} \in \mathbf{V}$, $p \in Q$, and $\phi \in Q$ then we decompose these spaces as:

$$\mathbf{V} = \mathbf{V}^c \oplus \mathbf{V}^f \qquad \text{and} \qquad Q = Q^c \oplus Q^f, \tag{25}$$

where $\overline{\mathbf{V}}$ and $\overline{Q}$ are the cG(r) subspaces of $\mathbf{V}$ and Q, respectively, and the primed versions are the complements of the cG(r) subspaces in $\mathbf{V}$ and Q, respectively. We decompose the velocity and pressure as follows:

$$\mathbf{v} = \mathbf{v}^c + \mathbf{v}^f, \quad \phi = \phi^c + \phi^f, \quad c^s = c^{s,c} + c^{s,f}, \quad \text{and} \quad p = p^c + p^f, \tag{26}$$

where the *coarse scale* components are $\mathbf{v}^c \in \mathbf{V}^c$ and $p^c, \phi^c, c^{s,c} \in Q^c$, and the *fine scale* components are $\mathbf{v}^f \in \mathbf{V}^f$ and $p^f, \phi^f \in Q^f$. We define a projection operator, $\mathscr{P} : \mathbf{V} \to \mathbf{V}^c$, such that $\mathbf{v}^c = \mathscr{P}\{\mathbf{v}\}$ and $\mathbf{v}^f = \mathbf{v} - \mathscr{P}\{\mathbf{v}\}$. Similar operators decompose the other variables, p, ϕ, c^s.

Substituting these decompositions in the original variational form in definition 1 yields:

$$
\begin{aligned}
\text{Momentum Eqns:} \quad & \frac{1}{Sc}\left(w_i, \frac{\beta_0 v_i^{c,k+1} + \beta_1 v_i^{c,k} + \beta_2 v_i^{c,k-1}}{\delta t}\right) \\
& + \frac{1}{Sc}\left(w_i, \widetilde{v}_j^{k+1} \frac{\partial v_i^{c,k+1}}{\partial x_j}\right) - \frac{1}{Sc}\left(\frac{\partial w_i}{\partial x_j}, \widetilde{v}_j^{k+1} v_j^{f,k+1}\right) \\
& + \left(w_i, \frac{\partial \left(p^{c,k+1} + p^{f,k+1}\right)}{\partial x_i}\right) + \left(\frac{\partial w_i}{\partial x_j}, \frac{\partial v_i^{c,k+1}}{\partial x_j}\right) + \boxed{\left(\frac{\partial w_i}{\partial x_j}, \frac{\partial v_i^{f,k+1}}{\partial x_j}\right)} \\
& + \frac{\kappa}{2\Lambda^2}\left(w_i, \left(\sum \left(c^{s,c,k+1} + c^{s,f,k+1}\right) z^s\right) \frac{\partial \phi^{c,k+1}}{\partial x_i}\right) \\
& + \boxed{\frac{\kappa}{2\Lambda^2}\left(w_i, \left(\sum \left(c^{s,c,k+1} + c^{s,f,k+1}\right) z^s\right) \frac{\partial \phi^{f,k+1}}{\partial x_i}\right)} \\
& + \left(q, \frac{\partial v_i^{c,k+1}}{\partial x_i}\right) + \left(q, \frac{\partial v_i^{f,k+1}}{\partial x_i}\right) = 0,
\end{aligned}
\tag{27}
$$

$$
\begin{aligned}
\text{Poisson:} \quad & 2\Lambda \left(\frac{\partial q}{\partial x_i}, \frac{\partial \left(\phi^{c,k+1} + \phi^{f,k+1}\right)}{\partial x_i}\right)_\Omega + 2\Lambda \left(q, n_i \frac{\partial \left(\phi^{c,k+1} + \phi^{f,k+1}\right)}{\partial x_i}\right)_{\partial\Omega} \\
& - \left(q, \sum c^{s,c,k+1} z^s\right)_\Omega - \left(q, \sum c^{s,f,k+1} z^s\right)_\Omega = 0,
\end{aligned}
\tag{28}
$$

---

[1] Adaptive mesh refinement to capture small-scale instabilities also presents its challenges, primarily of constructing *a*posteriori error estimates for solutions to Navier-Stokes which is an open research field

$$\text{Nernst-Planck:} \quad \left(q, \frac{\beta_0 c^{s,c,k+1} + \beta_1 c^{s,c,k} + \beta_2 c^{s,c,k-1}}{\delta t}\right)_\Omega + \left(q, \widetilde{v}_i^k \frac{\partial \left(c^{s,c,k+1} + c^{s,f,k+1}\right)}{\partial x_i}\right)_\Omega$$

$$+ \left(\frac{\partial q}{\partial x_i}, \frac{\partial \left(c^{s,c,k+1} + c^{s,f,k+1}\right)}{\partial x_i} + z^s \left(c^{s,c,k+1} + c^{s,f,k+1}\right) \frac{\partial \left(\phi^{c,k+1} + \phi^{f,k+1}\right)}{\partial x_i}\right)_\Omega$$

$$- \left(q, \hat{n}_i \left(\frac{\partial \left(c^{s,c,k+1} + c^{s,f,k+1}\right)}{\partial x_i} + z^s \left(c^{s,c,k+1} + c^{s,f,k+1}\right) \frac{\partial \left(\phi^{c,k+1} + \phi^{f,k+1}\right)}{\partial x_i}\right)\right)_{\partial\Omega} = 0, \tag{29}$$

where $\mathbf{w}, \mathbf{v}^c, \in \mathscr{P}\mathbf{H}^r(\Omega)$, p^c, $\phi^c \in \mathscr{P}H^r(\Omega)$, $\mathbf{v}^f \in (\mathscr{I} - \mathscr{P})\mathbf{H}^r(\Omega)$, $\phi^f, c^{s,f}, p^f \in (\mathscr{I} - \mathscr{P})H^r(\Omega)$, and $c^{s,c}, q \in \mathscr{P}H^r(\Omega)$. Here $\mathscr{I}$ is the identity operator, and $\mathscr{P}$ is the projection operator.

We can further simplify eq. (29),

$$\left(q, \frac{\beta_0 c^{s,c,k+1} + \beta_1 c^{s,c,k} + \beta_2 c^{s,c,k-1}}{\delta t}\right)_\Omega + \left(q, \widetilde{v}_i^k \frac{\partial \left(c^{s,c,k+1} + c^{s,f,k+1}\right)}{\partial x_i}\right)_\Omega$$

$$+ \left(\frac{\partial q}{\partial x_i}, \frac{\partial \left(c^{s,c,k+1} + c^{s,f,k+1}\right)}{\partial x_i} + z^s \left(c^{s,c,k+1} + c^{s,f,k+1}\right) \frac{\partial \left(\phi^{c,k+1} + \phi^{f,k+1}\right)}{\partial x_i}\right)_\Omega \tag{30}$$

$$- \left(q, \hat{n}_i \left(\frac{\partial \left(c^{s,c,k+1} + c^{s,f,k+1}\right)}{\partial x_i} + z^s \left(c^{s,c,k+1} + c^{s,f,k+1}\right) \frac{\partial \left(\phi^{c,k+1} + \phi^{f,k+1}\right)}{\partial x_i}\right)\right)_{\partial\Omega} = 0,$$

$$\implies \quad \left(q, \frac{\beta_0 c^{s,c,k+1} + \beta_1 c^{s,c,k} + \beta_2 c^{s,c,k-1}}{\delta t}\right)_\Omega + \left(q, \widetilde{v}_i^k \frac{\partial c^{s,c}}{\partial x_i}\right)_\Omega + \left(q, \widetilde{v}_i^k \frac{\partial c^{s,f}}{\partial x_i}\right)_\Omega$$

$$+ \left(\frac{\partial q}{\partial x_i}, \frac{\partial c^{s,c,k+1}}{\partial x_i}\right)_\Omega + \boxed{\left(\frac{\partial q}{\partial x_i}, \frac{\partial c^{s,f,k+1}}{\partial x_i}\right)_\Omega}$$

$$+ \left(\frac{\partial q}{\partial x_i}, z^s c^{s,c,k+1} \frac{\partial \phi^{c,k+1}}{\partial x_i}\right)_\Omega + \left(\frac{\partial q}{\partial x_i}, z^s c^{s,f,k+1} \frac{\partial \phi^{c,k+1}}{\partial x_i}\right)_\Omega$$

$$+ \boxed{\left(\frac{\partial q}{\partial x_i}, z^s c^{s,c,k+1} \frac{\partial \phi^{f,k+1}}{\partial x_i}\right)_\Omega} + \boxed{\left(\frac{\partial q}{\partial x_i}, z^s c^{s,f,k+1} \frac{\partial \phi^{f,k+1}}{\partial x_i}\right)_\Omega} \tag{31}$$

$$- \left(q, n_i \frac{\partial c^{s,c,k+1}}{\partial x_i}\right)_{\partial\Omega} - \boxed{\left(q, n_i \frac{\partial c^{s,f,k+1}}{\partial x_i}\right)_{\partial\Omega}}$$

$$- \left(q, n_i z^s c^{s,c,k+1} \frac{\partial \phi^{c,k+1}}{\partial x_i}\right)_{\partial\Omega} - \boxed{\left(q, n_i z^s c^{s,f,k+1} \frac{\partial \phi^{c,k+1}}{\partial x_i}\right)_{\partial\Omega}}$$

$$- \boxed{\left(q, n_i z^s c^{s,c,k+1} \frac{\partial \phi^{f,k+1}}{\partial x_i}\right)_{\partial\Omega}} - \boxed{\left(q, n_i z^s c^{s,f,k+1} \frac{\partial \phi^{f,k+1}}{\partial x_i}\right)_{\partial\Omega}}$$

$$= 0,$$

We set the boxed terms to zero (see next paragraph, and also, Table. 2). These assumptions reduce

the Nernst-Plank equations to the following,

Nernst-Planck:
$$\left(q, \frac{\beta_0 c^{s,c,k+1} + \beta_1 c^{s,c,k} + \beta_2 c^{s,c,k-1}}{\delta t}\right)_{\Omega} + \left(q, \widetilde{v}_i^k \frac{\partial c^{s,c,k+1}}{\partial x_i}\right)_{\Omega} + \left(q, \widetilde{v}_i^k \frac{\partial c^{s,f,k+1}}{\partial x_i}\right)_{\Omega}$$

$$+ \left(\frac{\partial q}{\partial x_i}, \frac{\partial c^{s,c,k+1}}{\partial x_i}\right)_{\Omega} + \left(\frac{\partial q}{\partial x_i}, z^s c^{s,c,k+1} \frac{\partial \phi^{c,k+1}}{\partial x_i}\right)_{\Omega} + \left(\frac{\partial q}{\partial x_i}, z^s c^{s,f,k+1} \frac{\partial \phi^{c,k+1}}{\partial x_i}\right)_{\Omega}$$

$$- \left(q, n_i \frac{\partial c^{s,c,k+1}}{\partial x_i}\right)_{\partial\Omega} - \left(q, n_i z^s c^{s,c,k+1} \frac{\partial \phi^{c,k+1}}{\partial x_i}\right)_{\partial\Omega} = 0$$

$$(32)$$

$$\implies \left(q, \frac{\beta_0 c^{s,c,k+1} + \beta_1 c^{s,c,k} + \beta_2 c^{s,c,k-1}}{\delta t}\right)_{\Omega} + \left(q, \widetilde{v}_i^k \frac{\partial c^{s,c,k+1}}{\partial x_i}\right)_{\Omega} - \left(\frac{\partial q}{\partial x_i}, \widetilde{v}_i^k c^{s,f,k+1}\right)_{\Omega}$$

$$+ \left(\frac{\partial q}{\partial x_i}, \frac{\partial c^{s,c,k+1}}{\partial x_i}\right)_{\Omega} + \left(\frac{\partial q}{\partial x_i}, z^s c^{s,c,k+1} \frac{\partial \phi^{c,k+1}}{\partial x_i}\right)_{\Omega} + \left(\frac{\partial q}{\partial x_i}, z^s c^{s,f,k+1} \frac{\partial \phi^{c,k+1}}{\partial x_i}\right)_{\Omega}$$

$$+ \boxed{\left(q, n_i \widetilde{v}_i^k c^{s,f,k+1}\right)_{\partial\Omega}} - \left(q, n_i \frac{\partial c^{s,c,k+1}}{\partial x_i}\right)_{\partial\Omega} - \left(q, n_i z^s c^{s,c,k+1} \frac{\partial \phi^{c,k+1}}{\partial x_i}\right)_{\partial\Omega} = 0.$$

$$(33)$$

Table 2 lists the various boxed terms in the coupled set of NS-PNP equations that are set to
zero, along with the rationale for setting them to zero. We remind the reader that these terms are
set to zero based on well-established assumptions from VMS approaches [52, 54, 55], as well as
moderate assumptions on smoothness of the potential (which allows us to set ϕ^f to zero), and that
the fine-scale variables for concentration and potential are zero at the boundary.

Equation	Terms	Rational for assumption
Momentum equations	$\left(\dfrac{\partial w_i}{\partial x_j},\ \dfrac{\partial v_i^{f,k+1}}{\partial x_j}\right)_\Omega$	*Projection:* Orthogonality conditions from the projection decomposition, as $w_i \in \mathscr{P}\mathbf{H}^r(\Omega)$ and $v_i^{f,k+1} \in (\mathscr{I} - \mathscr{P})\mathbf{H}^r(\Omega)$
Momentum equations	$\dfrac{\kappa}{2\Lambda^2}\left(w_i,\ \left(\sum\left(c^{s,c,k+1} + c^{s,f,k+1}\right)z^s\right)\dfrac{\partial \phi^{f,k+1}}{\partial x_i}\right)_\Omega$	$\phi^{f,k+1}$ assumed to be zero
Nernst-Planck equations	$\left(q,\ n_i\widetilde{v}_i^k c^{s,f,k+1}\right)_{\partial\Omega}$	Depends on the boundary condition, could be zero by either a Dirichlet condition of velocity or a Dirichlet condition of concentration
Nernst-Planck equations	$\left(\dfrac{\partial q}{\partial x_i},\ \dfrac{\partial c^{s,f,k+1}}{\partial x_i}\right)_\Omega$	*Projection:* Orthogonality conditions from the projection decomposition, as $q \in \mathscr{P}H^r(\Omega)$ and $c^{s,f,k+1} \in (\mathscr{I} - \mathscr{P})H^r(\Omega)$
Nernst-Planck equations	$\left(\dfrac{\partial q}{\partial x_i},\ z^s c^{s,c,k+1}\ \dfrac{\partial \phi^{f,k+1}}{\partial x_i}\right)_\Omega$	$\phi^{f,k+1}$ assumed to be zero
Nernst-Planck equations	$\left(\dfrac{\partial q}{\partial x_i},\ z^s c^{s,f,k+1}\ \dfrac{\partial \phi^{f,k+1}}{\partial x_i}\right)_\Omega$	$\phi^{f,k+1}$ assumed to be zero
Nernst-Planck equations	$\left(q,\ n_i\dfrac{\partial c^{s,f,k+1}}{\partial x_i}\right)_{\partial\Omega}$	flux of $c^{s,f,k+1}$ assumed to be zero on boundaries
Nernst-Planck equations	$\left(q,\ n_i z^s c^{s,f,k+1}\ \dfrac{\partial \phi^{c,k+1}}{\partial x_i}\right)_{\partial\Omega}$	$\phi^{f,k+1}$ assumed to be zero
Nernst-Planck equations	$\left(q,\ n_i z^s c^{s,c,k+1}\ \dfrac{\partial \phi^{f,k+1}}{\partial x_i}\right)_{\partial\Omega}$	$\phi^{f,k+1}$ assumed to be zero
Nernst-Planck equations	$\left(q,\ n_i z^s c^{s,f,k+1}\ \dfrac{\partial \phi^{f,k+1}}{\partial x_i}\right)_{\partial\Omega}$	$\phi^{f,k+1}$ assumed to be zero
Poisson equations	$2\Lambda\left(\dfrac{\partial q}{\partial x_i},\ \dfrac{\partial \phi^{f,k+1}}{\partial x_i}\right)_\Omega$	$\phi^{f,k+1}$ assumed to be zero
Poisson equations	$2\Lambda\left(q,\ n_i\dfrac{\partial \phi^{f,k+1}}{\partial x_i}\right)_{\partial\Omega}$	$\phi^{f,k+1}$ assumed to be zero

Table 2: Table to test captions and labels.

With all the simplifications listed in Table 2 we can now write the fully discrete variational form for the NS-PNP equations.

Let $(\cdot, \cdot)$ be the standard L^2 inner product. We state the time-discrete variational problem as follows: find $\mathbf{v}^{c,k+1}, \in \mathscr{P}\mathbf{H}^r(\Omega)$, and $p^{c,k+1}$, $c^{s,c,k+1}(\mathbf{x})$, $\phi^{c,k+1} \in \mathscr{P}H^r(\Omega)$ such that

$$\text{Momentum Eqns:} \quad \frac{1}{Sc}\left(w_i, \frac{\beta_0 v_i^{c,k+1} + \beta_1 v_i^{c,k} + \beta_2 v_i^{c,k-1}}{\delta t}\right)$$

$$+ \frac{1}{Sc}\left(w_i, \widetilde{v}_j^{k+1}\frac{\partial v_i^{c,k+1}}{\partial x_j}\right) - \frac{1}{Sc}\left(\frac{\partial w_i}{\partial x_j}, \widetilde{v}_j^{k+1}v_j^{f,k+1}\right)$$

$$+ \left(w_i, \frac{\partial\left(p^{c,k+1} + p^{f,k+1}\right)}{\partial x_i}\right) + \left(\frac{\partial w_i}{\partial x_j}, \frac{\partial v_i^{c,k+1}}{\partial x_j}\right) \tag{34}$$

$$+ \frac{\kappa}{2\Lambda^2}\left(w_i, \left(\sum c^{s,k+1}z^s\right)\frac{\partial\phi^{c,k+1}}{\partial x_i}\right) = 0,$$

$$\text{Solenoidality:} \quad \left(q, \frac{\partial v_i^{c,k+1}}{\partial x_i}\right) + \left(\frac{\partial q}{\partial x_i}, v_i^{f,k+1}\right) = 0, \tag{35}$$

$$\text{Poisson:} \quad 2\Lambda\left(\frac{\partial q}{\partial x_i}, \frac{\partial\phi^{c,k+1}}{\partial x_i}\right)_\Omega - 2\Lambda\left(q, n_i\frac{\partial\phi^{c,k+1}}{\partial x_i}\right)_{\partial\Omega}$$

$$- \left(q, \sum c^{s,c,k+1}z^s\right)_\Omega - \left(q, \sum c^{s,f,k+1}z^s\right)_\Omega = 0, \tag{36}$$

$$\text{Nernst-Planck:} \quad \left(q, \frac{\beta_0 c^{s,c,k+1} + \beta_1 c^{s,c,k} + \beta_2 c^{s,c,k-1}}{\delta t}\right)_\Omega$$

$$+ \left(q, \widetilde{v}_i^k\frac{\partial c^{s,c,k+1}}{\partial x_i}\right)_\Omega - \left(\frac{\partial q}{\partial x_i}, \widetilde{v}_i^k c^{s,f,k+1}\right)_\Omega$$

$$+ \left(\frac{\partial q}{\partial x_i}, z^s c^{s,c,k+1}\frac{\partial\phi^{c,k+1}}{\partial x_i}\right)_\Omega + \left(\frac{\partial q}{\partial x_i}, z^s c^{s,f,k+1}\frac{\partial\phi^{c,k+1}}{\partial x_i}\right)_\Omega \tag{37}$$

$$+ \left(\frac{\partial q}{\partial x_i}, \frac{\partial c^{s,c,k+1}}{\partial x_i}\right)_\Omega$$

$$- \left(q, n_i\frac{\partial c^{s,c,k+1}}{\partial x_i}\right)_{\partial\Omega} - \left(q, n_i z^s c^{s,c,k+1}\frac{\partial\phi^{c,k+1}}{\partial x_i}\right)_{\partial\Omega} = 0.$$

$\forall \mathbf{w} \in \mathscr{P}\mathbf{H}^r(\Omega)$, $q \in \mathscr{P}H^r(\Omega)$
, and $\mathbf{v}^{f,k+1} \in (\mathscr{I} - \mathscr{P})\mathbf{H}^r(\Omega)$, $c^{s,f,k+1}, p^{f,k+1} \in (\mathscr{I} - \mathscr{P})H^r(\Omega)$
, given $\mathbf{v}^k$, $\mathbf{v}^{k-1} \in \mathbf{H}^r(\Omega)$, and $\phi^k, \phi^{k-1}, c^{s,k}, c^{s,k} \in H^r(\Omega)$.

Note that the above variational problem is not closed as the fine-scale velocities, pressure, and ion concentrations are unknown. To close the system, we use the *residual-based approximation* proposed in Bazilevs et al. [54] for the fine-scale components. Defining $\mathcal{R}_m$, $\mathcal{R}_{sol}$, and $\mathcal{R}_{c^s}$ as the residuals of the momentum, solenoidility and Nernst-Plank equations, the fine scale components are:

$$v_i^f = -\tau_m \mathcal{R}_m\left(v_i^c, p^c, c^{s,c}\right), \qquad p^f = -\tau_{sol}\mathcal{R}_{sol}(v_i^c), \qquad \text{and} \qquad c^{s,f} = -\tau_{c^s}\mathcal{R}_{c^s}\left(c^{s,c}, v_i^c, \phi^c\right), \tag{38}$$

13

where,

$$\tau_m = \left(\frac{4}{\Delta t^2} + v_i^c G_{ij} v_j^c + C_I \left(\frac{1}{Re} \right)^2 G_{ij} G_{ij} \right)^{-1/2}, \tag{39}$$

$$\tau_{sol} = \frac{1}{tr(G_{ij})\tau_m}, \tag{40}$$

$$\tau_{c^s} = \left(\frac{4}{\Delta t^2} + v_i^c G_{ij} v_j^c + C_I G_{ij} G_{ij} \right)^{-1/2}. \tag{41}$$

Here we set C_I and C_ϕ for all our simulations to 6, and $G_{ij} = \sum_{k=1}^{3} \partial \xi_k / \partial x_i \partial \xi_k / \partial x_j$ is a mesh-based tensor that accounts for the inverse mapping ($\partial \xi_k / \partial x_i$) between the parametric and the physical domain of the element. For octrees, with equal aspect ratio ($\Delta x = \Delta y = \Delta z = h$), such a transformation simplifies G_{ij} to $(2/h)^2$, where h is the element's size. Subsequently, the final fully-discrete variational form that is solved can be written as follows.

14

> **Definition 3**
>
> Let $(\cdot, \cdot)$ be the standard L^2 inner product. We state the time-discrete variational problem as follows: find $\mathbf{v}^{c,k+1}, \in \mathscr{P}\mathbf{H}^r(\Omega)$, and $p^{c,k+1}$, $c^{s,c,k+1}(\mathbf{x})$, $\phi^{c,k+1} \in \mathscr{P}H^r(\Omega)$ such that
>
> Momentum Eqns:
> $$\frac{1}{Sc}\left(w_i, \frac{\beta_0 v_i^{c,k+1} + \beta_1 v_i^{c,k} + \beta_2 v_i^{c,k-1}}{\delta t}\right)$$
>
> $$+ \frac{1}{Sc}\left(w_i, \widetilde{v}_j^{k+1}\frac{\partial v_i^{c,k+1}}{\partial x_j}\right) + \frac{1}{Sc}\left(\frac{\partial w_i}{\partial x_j}, \widetilde{v}_j^{k+1}\tau_m \mathcal{R}_m\left(v_i^{c,k+1}, p^{c,k+1}, c^{s,c,k+1}\right)\right)$$
>
> $$+ \left(w_i, \frac{\partial p^{c,k+1}}{\partial x_i}\right) + \left(\frac{\partial w_i}{\partial x_i}, \tau_{sol}\mathcal{R}_{sol}\left(v_i^{c,k+1}\right)\right)$$
>
> $$+ \left(\frac{\partial w_i}{\partial x_j}, \frac{\partial v_i^{c,k+1}}{\partial x_j}\right)$$
>
> $$+ \frac{\kappa}{2\Lambda^2}\left(w_i, \left(\sum c^{s,k+1}z^s\right)\frac{\partial \phi^{c,k+1}}{\partial x_i}\right) = 0,$$
>
> $$\tag{42}$$
>
> Solenoidality: $\left(q, \frac{\partial v_i^{c,k+1}}{\partial x_i}\right) - \left(\frac{\partial q}{\partial x_i}q, \tau_m \mathcal{R}_m\left(v_i^{c,k+1}, p^{c,k+1}, c^{s,c,k+1}\right)\right) = 0,$ $\tag{43}$
>
> Poisson: $2\Lambda\left(\frac{\partial q}{\partial x_i}, \frac{\partial \phi^{c,k+1}}{\partial x_i}\right)_\Omega - 2\Lambda\left(q, n_i \frac{\partial \phi^{c,k+1}}{\partial x_i}\right)_{\partial\Omega}$
>
> $$- \left(q, \sum z^s c^{s,c,k+1}\right)_\Omega + \left(q, \sum z^s \tau_{c^s} \mathcal{R}_{c^s}\left(v_i^{c,k+1}, \phi^{c,k+1}\right)\right)_\Omega = 0,$$
>
> $$\tag{44}$$
>
> Nernst-Planck: $\left(q, \frac{\beta_0 c^{s,c,k+1} + \beta_1 c^{s,c,k} + \beta_2 c^{s,c,k-1}}{\delta t}\right)_\Omega$
>
> $$+ \left(q, \widetilde{v}_i^k \frac{\partial c^{s,c,k+1}}{\partial x_i}\right)_\Omega + \left(\frac{\partial q}{\partial x_i}, \widetilde{v}_i^k \tau_{c^s} \mathcal{R}_{c^s}\left(v_i^{c,k+1}, \phi^{c,k+1}\right)\right)_\Omega$$
>
> $$+ \left(\frac{\partial q}{\partial x_i}, z^s c^{s,c,k+1}\frac{\partial \phi^{c,k+1}}{\partial x_i}\right)_\Omega - \left(\frac{\partial q}{\partial x_i}, z^s \tau_{c^s}\mathcal{R}_{c^s}\left(v_i^{c,k+1}, \phi^{c,k+1}\right)\frac{\partial \phi^{c,k+1}}{\partial x_i}\right)_\Omega$$
>
> $$+ \left(\frac{\partial q}{\partial x_i}, \frac{\partial c^{s,c,k+1}}{\partial x_i}\right)_\Omega$$
>
> $$- \left(q, n_i \frac{\partial c^{s,c,k+1}}{\partial x_i}\right)_{\partial\Omega} - \left(q, n_i z^s c^{s,c,k+1}\frac{\partial \phi^{c,k+1}}{\partial x_i}\right)_{\partial\Omega} = 0.$$
>
> $$\tag{45}$$
>
> $\forall \mathbf{w} \in \mathscr{P}\mathbf{H}^r(\Omega), q \in \mathscr{P}H^r(\Omega)$
> , and $\mathbf{v}^{f,k+1} \in (\mathscr{I} - \mathscr{P})\mathbf{H}^r(\Omega), c^{s,f,k+1}, p^{f,k+1} \in (\mathscr{I} - \mathscr{P})H^r(\Omega)$
> , given $\mathbf{v}^k$, $\mathbf{v}^{k-1} \in \mathbf{H}^r(\Omega)$, and $\phi^k, \phi^{k-1}, c^{s,k}, c^{s,k-1} \in H^r(\Omega)$.

4. Solution strategy and design of the numerical framework

4.1. Solution strategy

It is important to note that because we are using a block solution method, the fully discrete Navier-Stokes equations, eqs. (42) to (43), and the Poisson Nernst Planck equations, eqs. (44) to (45), are solved as two different sub-problems. Note that the NS (eqs. (42) to (43)) is a linear system, whereas, PNP (eqs. (44) to (45)) is a non-linear system. We use the Newton method to reduce the non-linear system (eqs. (42) to (43)) to an iteration of linear problems. Symbolically, we can write this nonlinear algebraic system as

$$T_i\left(U_1^k, U_2^k, \ldots, U_n^k\right) = 0, \tag{46}$$

where $\mathbf{U}^k$ is a finite-dimensional vector that contains all of the degrees of freedom at the discrete-time level t^k. In the system of eqs. (42) and (43), $\mathbf{U}^k$ contains ion concentrations and electric potential at time level k. Then the Newton iteration can be posed as,

$$A_{ij}^{m,k}\, \delta U_j^{m,k} = -T_i\left(U_1^{m,k}, U_2^{m,k}, \ldots, U_n^{m,k}\right), \qquad A_{ij}^{m,k} := \frac{\partial}{\partial U_j} F_i\left(U_1^{m,k}, U_2^{m,k}, \ldots, U_n^{m,k}\right), \tag{47}$$

where $U_j^{m,k}$ is the vector containing all the degrees of freedom at the kth time step and at the mth Newton iteration. $\delta U_j^{m,k}$ is the "variation" vector that will be used to update the current Newton iteration guess:

$$U_j^{m+1,k} = U_j^{m,k} + \delta U_j^{m,k}. \tag{48}$$

and $A_{ij}^{m,k}$ is the Jacobian matrix computed analytically compute by calculating the variations (partial derivatives) of the operators with respect to the degrees of freedom. The iterative procedure begins with an initial guess which is set to the solution from the previous time step:

$$U_i^{0,k} = U_i^{k-1}, \tag{49}$$

and ends once we reach the desired tolerance:

$$\|\delta U_j^{m,k}\| \leq \text{TOL}. \tag{50}$$

The block strategy for solving the system is given in Fig. 1. The flow chart in fig. 1 shows that the linear semi-implicit Navier Stokes system is solved first from the available data from the previous timestep. Subsequently, the Poisson Nernst-Planck system is solved from the data from the previous timestep and the first block of Navier-Stokes. The block iteration is repeated until a desired convergance is reached. Numerical experiments reveal that 2 block iterations produces tight convergence for all examples; with 1 block iteration often providing good results for most examples.

4.2. Software design

The software is designed in a layer-by-layer fashion. The numerical simulation presented in this work is implemented on top of massively parallel framework DENDRITE-KT. DENDRITE-KT uses DENDRO-KT for adaptive octree mesh generation and PETSC for linear algebra solver by utilizing KSP (Krylov Subspace) context for solving linear system of equations and SNES context for Newton iteration. DENDRO-KT allows allows for targeted, dynamic mesh refinement based on either the location or *aposteriori* estimates.

16

Known fields at
some timestep k:
$\mathbf{v}^k$, $\mathbf{v}^{k-1}$, p^k, ϕ^k,
ϕ^{k-1}, $c^{s,k}$, $c^{s,k-1}$,
$\text{block}_{\text{iter}} : \ell = 0$

Semi-Implicit: Solve Navier-Stokes and
update the fields (eqs. (42) to (43)):
$\mathbf{v}^{k+1(\ell)}, p^{k+1(\ell)} \leftarrow \mathbf{v}^k, p^k, \phi^k, c^{s,k} \quad p^{k+1(\ell)} \leftarrow p^k$

Fully-Implicit: Solve Poisson and Nernst-Planck
equations and update the fields (eqs. (44) to (45)):
$c^{s,k+1(\ell)} \leftarrow c^{s,k}, \mathbf{v}^{k+1(\ell)}, \mathbf{v}^k$ and $\quad \phi^{k+1(\ell)} \leftarrow \phi^k, c^{s,k+1(\ell)}, c^{s,k}$

$\text{block}_{\text{iter}} : \ell = \ell + 1$

if $\text{block}_{\text{iter}} > 1$ and
$\max \left\| \mathbf{U}^{k+1(\ell)} - \mathbf{U}^{k+1(\ell-1)} \right\| <$
$\text{block}_{\text{tol}}$, where $\mathbf{U}^{k+1}$
is a vector containing
$\mathbf{v}^{k+1(l)}, p^{k+1(l)}, c^{s,k+1(l)}, \phi^{k+1(l)}$

NO

YES, for $\ell = m$

Solution at current timestep $k + 1$ ($\ell = m$): $\mathbf{v}^{k+1} = \mathbf{v}^{k+1(m)}, , p^{k+1} = p^{k+1(m)}, , \phi^{k+1} = \phi^{k+1(m)}, c^{s,k+1} = c^{s,k+1(m)}$

Figure 1: Flowchart for the block iteration technique as described in section 4.1 .

The organization of the overall framework is illustrated in Fig. 2. The yellow layers represent the computational framework. The modeling framework - shown as three blocks on top of the computational framework, represents the fully discrete scheme presented in section 3. The non-linear solve for the PNP system (eqs. (44) to (45)) is solved by coupling the data structures on the octree meshing framework with Petsc using the SNES context. Subsequently, the inner linear solves required for the PNP system and the NS system (eqs. (42) to (43)) are solved using the KSP construct. This allows us to exploit the plethora of preconditioner and linear iterative solvers in Petsc. The final solution vectors are saved in the parallel VTK format, which makes visualization using ParaView straightforward.

Dendro-KT meshing framework: An "octant" represents the fundamental building block of the octree mesh. At the root of the octree, an octant is a cube that encompasses the full domain. In order to construct the octree, all p compute processes start at the root node. To avoid communication during the refinement stage, we perform redundant computations on all p processes. Starting from the root node, all processes refine (similar to the sequential code) until at least $\mathcal{O}(p)$ octants are produced. Then using a weighted space-filling-curve (SFC) based partitioning, we partition the octants across all processes. Further, proceeding in a top-down fashion, an octant is refined based on user-specified criteria. The refinement criteria is a user-specified function that takes the coordinates of the octant and the associated values, and returns true or false. Since the refinement happens in an element-local fashion, this step is embarrassingly parallel. In distributed memory, the initial top-down tree construction (which describes the mesh) also enables an efficient partitioning of the domain across an arbitrary number of processes.

The key distinguishing factor for Dendro-KT, as compared to other octree libraries [42, 56, 57], is the ability to carve out any arbitrarily shaped object based on a simple Active - InActive classification of a point $\in \mathbb{R}^d$, leading to the generation of *incomplete* octree. An element is said to be Active, if all the nodes of the element falls within the active region of the domain Ω and InActive if all the nodes falls within the inactive region. If some of the nodes fall within the active region and some within the inactive, the element is marked Intercepted. The basic idea of Dendro-KT is to retain the Active and Intercepted elements and remove the InActive elements. Such a construction leads to generation of octree that is *incomplete*. An octree is called incomplete if siblings of at least one octant (at any given level) are missing. During the top-down construction, if any given octant falls into the InActive region of the domain, then the given octant is not further considered a candidate for refinement. This introduces a very efficient way to generate octrees by pruning the tree at a coarser level. Additionally, incomplete octrees provide saving in total number of degrees of freedom to be solve, in comparison to traditional complete octrees. This translates to additional savings in time-to-solve as well as conditioning of the matrix. We refer the interested readers to our previous work [58, 59] for further details of incomplete octree construction and scalability performance.

FEM operations: Dendro-KT supports both matrix and matrix-free computations. To prevent indirect memory access, Dendro-KT does not store any elemental to global map data structure but relies on performing top-down and bottom-up traversals of the mesh tree. The top-down and bottom-up traversals can be thought of as scatter and gather operations, respectively.

The top-down phase selectively copies nodes from coarser to finer levels until the leaf level is reached. We create buckets for all child subtrees. Looping through the nodes, a node is copied into a bucket if the node is incident on the child subtree corresponding to that bucket. A node that is incident on multiple child subtrees will be duplicated. By recursing on each child subtree and its corresponding bucket of incident nodes, we eventually reach the leaf level. Once the traversal reaches a leaf octant, the elemental nodes have been copied into a contiguous array. The elemental vector is computed directly without the use of an element-to-node map. The result is stored in a
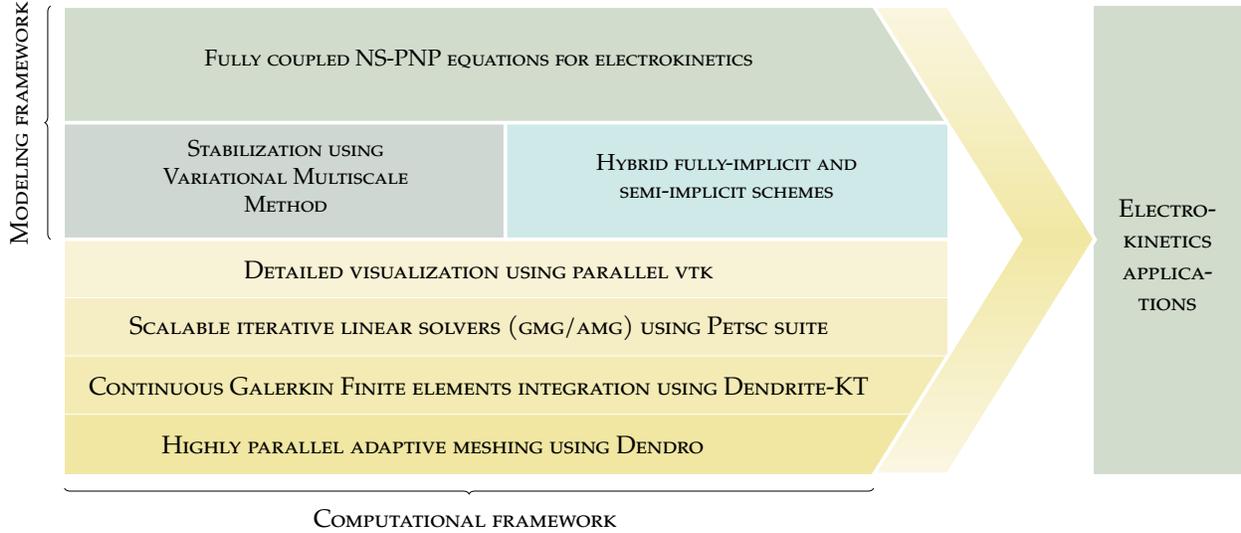
Figure 2: Design schematic of the parallel framework for solving NS-PNP.

contiguous output buffer the same size as the local elemental input vector.

After all child subtrees have been traversed, the bottom-up phase returns results from a finer to a coarser level. The parent subtree nodes are once again bucketed to child subtrees, but instead of the parent values being copied, the values of nodes from each child are accumulated into a parent output array. For any node that is incident on multiple child subtrees, the values from all node instances are summed to a single value. The global vector is assembled after the bottom-up phase executes at the root of the octree. A detailed description of this process is provided in our previous work, specifically Saurabh et al. [58], Ishii et al. [60], Khanwale et al. [61]

5. Results

5.1. Method of manufactured solutions for convergence analysis

We use the method of manufactured solutions to assess the temporal and spatial convergence of our proposed scheme. In this work, we restrict ourselves to a linear basis function ($r = 1$). We construct the appropriate forcing function to satisfy the analytical solution of the form:

$$
\begin{aligned}
u &= \cos(2t)\sin(2\pi x)\cos(2\pi y)\\
v &= -\cos(2t)\cos(2\pi x)\sin(2\pi y)\\
p &= \cos(2t)\sin(2\pi x)\cos(2\pi y)\\
\phi &= -\cos(2t)\cos(2\pi x)\sin(2\pi y)\\
c^+ &= \cos(2t)\cos(2\pi x)\sin(2\pi y)\\
c^- &= \cos(2t)\sin(2\pi x)\cos(2\pi y)
\end{aligned}
\tag{51}
$$

We solve the NS-PNP equations on a square domain $[0, 1]^2$, with Dirichlet conditions enforced on all boundaries. We note that the manufactured solution for the fluid velocity is divergence-free. Fig. 3 shows both the spatial and temporal discretization convergence results. For the spatial convergence analysis, we fixed the timestep Δt at 0.0157 and varied the spatial resolution. Next, to study the temporal convergence behavior, we chose the spatial resolution to be level 9 ($\Delta x = \Delta y =$

19

(a) Spatial convergence (b) Temporal convergence
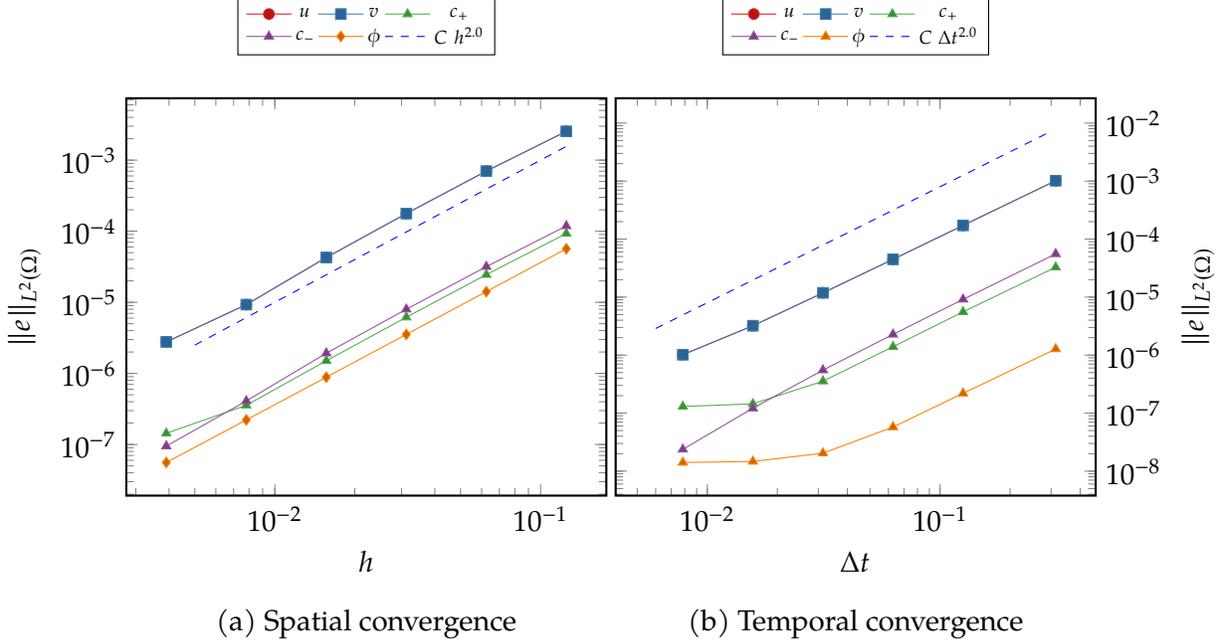
Figure 3: Convergence analysis using the method of manufactured solutions. (a), spatial, and (b), temporal convergence of the NS-PNP solver.

$1/2^9$). The L_2 error is reported at the final time of $t = \pi$. We observe an expected second-order
spatial (Fig. 3(a)) and temporal convergence (Fig. 3(a)). At an error of about $\mathcal{O}(10^{-7})$, we see the
flattening out of the error curves, especially in temporal convergence studies. This flattening can
be attributed to the errors from the spatial resolution limit starting to dominate the L_2 error. These
results indicate that the implementation exhibits the expected second-order spatial and temporal
convergence behavior.

5.2. Electro-Osmotic Flow

We next test our approach to model electroosmotic flow (EOF) in a straight channel by solving
the NS-PNP equations for monovalent binary electrolytes (i.e., $s = 2$, $z = 1$). EOF forms when an
electric field is applied across a channel with charged walls. The applied electric field drives fluid
flow in the boundary layer where the net charge is non-zero, resulting in the typical plug shaped
profile due to the shear stress. We simulate EOF in a 2-D straight channel having zeta potential (ζ_0)
of -2.77 against the channel center and a potential drop (0.3959) along the channel axis ($X = 10$).
The concentration at the inlet and outlet is set to 1.0, and no-mass transport is allowed across the
wall boundary. The non-slip boundary condition is applied at the channel wall, and, at the inlet
and outlet, $v_y = 0$, $p = 0$, and $\frac{\partial v_x}{\partial x} = 0$. The $Sc = \frac{\eta}{\rho D}$ was 6.87×10^2, and $\Lambda = \frac{\lambda}{L_{ch}}$ was 0.096.

Considering the symmetric nature of the velocity profile, only the bottom half of the channel
was calculated. The size of the mesh was 0.0156 near the bottom wall ($y \leq 0.7$) to resolve the
boundary layer and 0.0313 away from the wall ($y > 0.7$). Initially, only the PNP equations were
solved to obtain the initial condition with developed EDL, and then, the fully coupled NS-PNP
equations were solved to simulate EOF. A time step of $\Delta t = 1e-5$ was chosen. Around 100 timesteps
produce the expected plug profile.

The evolution of the boundary layer and the steady-state plug profile can be found at Fig. 4.

20
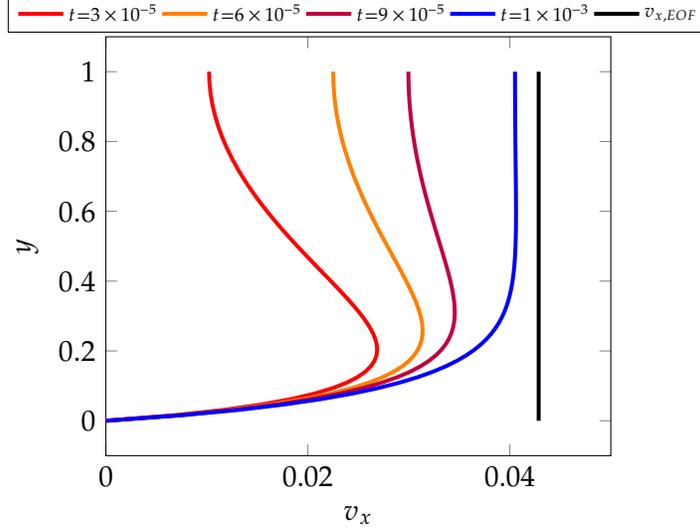
Figure 4: Evolution of velocity profile from EOF simulation and analytical solution.

The analytical solution of electroosmotic flow velocity is

$$v^*_{x,EOF} = -\frac{\varepsilon \zeta^*_0 E_x}{\eta}. \tag{52}$$

For the EOF simulation in this section, $\varepsilon = 7.083 \times 10^{-10}$ and $\eta = 8.9 \times 10^{-4}$. And the non-dimensional EOF velocity is

$$v_{x,EOF} = \frac{L_{ch}}{D} v^*_{x,EOF}. \tag{53}$$

Fig. 4 shows that as the flow develops, the plug flow profile approaches the analytical plug flow prediction of $v_{x,EOF}$. After the flow was fully developed, we found a good agreement between EOF simulation and analytical solution with less than 5% error.

5.3. Electro-convective instability

We next demonstrate electrokinetic transport near an ion-selective surface, which is a good benchmarking problem because 1) the problem can be found in a wide range of applications, 2) the length scale of the EDL near the surface requires an extremely small mesh size, which makes the problem a good test case for the proposed octree-based mesh, and 3) the turbulence-like characteristics trigger numerical instabilities, which necessitates numerical stabilization from VMS.

The simulation was performed for the transport of monovalent binary electrolytes in a rectangular domain whose dimension is 8×1. The top boundary is a reservoir at which the potential and the concentration of both species are fixed (Dirichlet). The ion-selective surface is located at the bottom boundary, where the potential is grounded. The cation concentration was $c^+ = 2$, and no anion flux was allowed across the ion-selective surface. A periodic boundary condition is applied to the side walls. Fig. 5 shows the schematic of the domain, and Table 3 lists the boundary conditions for the different variables. We consider two cases, one when a moderate potential difference of $\Delta\phi = 20$ is imposed across the domain, and another when a large potential difference of $\Delta\phi = 120$ is imposed. We anticipate significant electro-convective instabilities to occur in the second case.

Similar to the previous example, finer refinement was used near the ion-selective surface to resolve steep gradients in the boundary layer. The bottom part of the domain, extending from y =

21
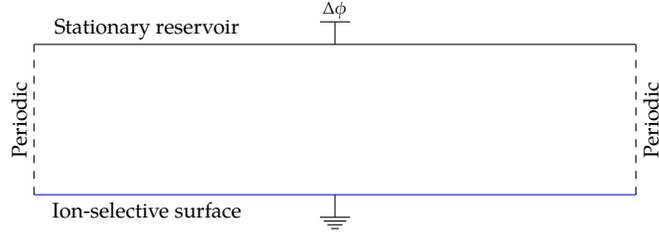
Figure 5: Schematic diagram (not on scale) for the electro-convective instability.

		Variable	Type	Value
NS	Top Wall	u	Dirichlet	0
		v	Dirichlet	0
	Bottom Wall	u	Dirichlet	0
		v	Dirichlet	0
	Side walls	Periodic		
PNP	Top Wall	ϕ	Dirichlet	20 or 120
		c_+	Dirichlet	1
		c_-	Dirichlet	1
	Bottom Wall	ϕ	Dirichlet	0
		c_+	Dirichlet	2
		c_-	Neumann	0
	Side walls	Periodic		

Table 3: Boundary condition for the electro-convective instabilty

0 to y = 0.1, consists of elements refined to level 13 ($\Delta x = \Delta y = 8/2^{13}$), while the rest of the region consists of elements refined to level 10 ($\Delta x = \Delta y = 8/2^{10}$). The setup resulted in a domain with approximately 1M cells. In contrast, an equivalent uniform mesh at the finest resolution would have $\sim$ 10M cells. The initial condition with fully developed EDL was generated by solving only the PNP equations, then randomly perturbing the resultant concentrations locally by 1% to initiate the instability before solving the fully coupled NS-PNP equations. The timestep was 10^{-2} for the case with potential difference, $\Delta\phi = 20$, and a time step of 10^{-4} for the case of potential difference $\Delta\phi = 120$.

We first compare the temporal evolution of the charge density ($c^+ - c^-$) and velocity fields under the imposition of the potential drops. This is shown in Fig. 6 for the $\Delta\phi = 20$ case and Fig. 7 for the $\Delta\phi = 120$ case. Once a potential drop is applied, the ion concentration profile near the ion-selective surface forms an electric double layer (EDL) and diffusion layer (DL). Depending on the level of the potential drop, the extended space charge layer (ESC) may form between EDL and DL [16]. When $\Delta\phi = 20$, the ESC is not formed, and the magnitude of convection was insufficient to trigger instabilities. A series of counter-rotating vortices are observed in Fig. 6. On the other hand, an ESC was observed in the initial stage of $\Delta\phi = 120$. The interplay between ESC and convection triggered electrohydrodynamic instability, as reported in Druzgalski et al. [16]. As the simulation proceeds, the development of electrohydrodynamic instability becomes even more evident. We note that the average velocity at $\Delta\phi = 120$ was greater than that of $\Delta\phi = 20$ case by two orders of magnitude.

We next extract quantitative properties for comparison. The current measured on the boundary is an often used property, as it is the easiest property to experimentally measure. Fig. 8 (a) shows the temporal variation of the magnitude of the net species flux, $|j_T^\pm|$, through the top boundary, calculated as

$$
j_T^\pm = -\frac{1}{L_T} \sum_{l=1}^{N_T} \left[\left(q,\ \hat{n}_T \left(\frac{\partial c^{+,t}}{\partial x_i} + z^+ c^{+,t} \frac{\partial \phi^t}{\partial x_i} \right) \right)_{\Gamma_l} - \left(q,\ \hat{n}_T \left(\frac{\partial c^{-,t}}{\partial x_i} + z^- c^{-,t} \frac{\partial \phi^t}{\partial x_i} \right) \right)_{\Gamma_l} \right], \qquad (54)
$$

where L_T, N_T, $\hat{n}_T$, and $\Gamma = \partial\Omega_\Gamma$ are the length of the top boundary, the number of the top boundary elements, the normal vector to the top boundary, and the top boundary, respectively. We see that, in the absence of electro-convective instabilities, the current (for the $\Delta\phi = 20$ case) was uniform over time, as expected in the absence of ESC and not enough convection to perturb established EDL. In contrast, the significant current fluctuations was observed for the $\Delta\phi = 120$ case due to the instability.

We finally plot $x-$averaged field values for the potential (Fig. 8 (b)), concentration (Fig. 8 (c)) and charge density (Fig. 8 (d)). Note the logarithmic axis in these figures to ensure that the variation close to the ion-selective surface are emphasized. These figures also allow detailed comparison with previous DNS simulations of the same case by Druzgalski et al. [16], which shows excellent agreement. Note that our numerical scheme allows three orders of magnitude larger time steps as compared to the benchmarking problem by Druzgalski et al. [16], with identical results.

23
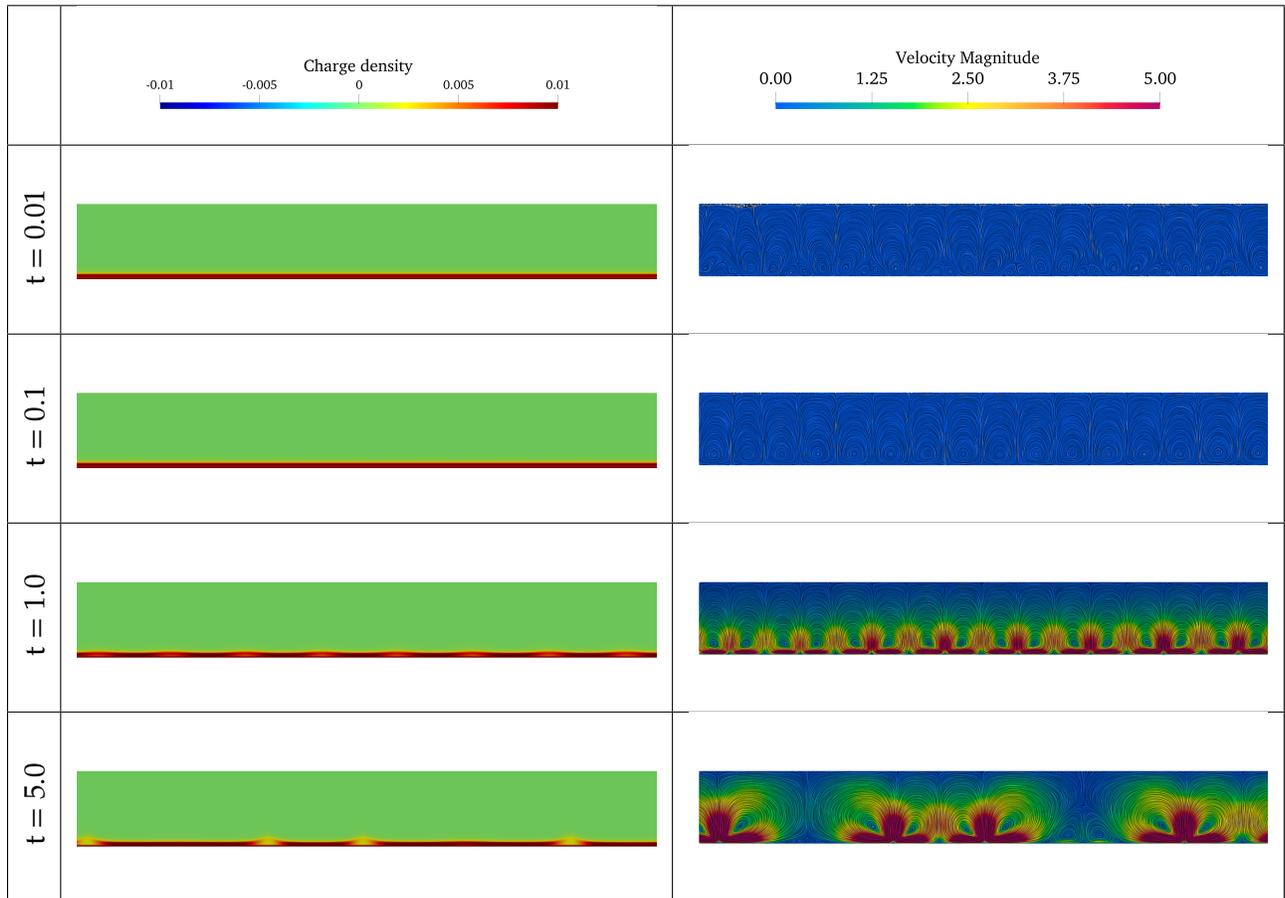
Figure 6: Contour plots of charge density and velocity magnitudes at different times for $\Delta\phi = 20$.
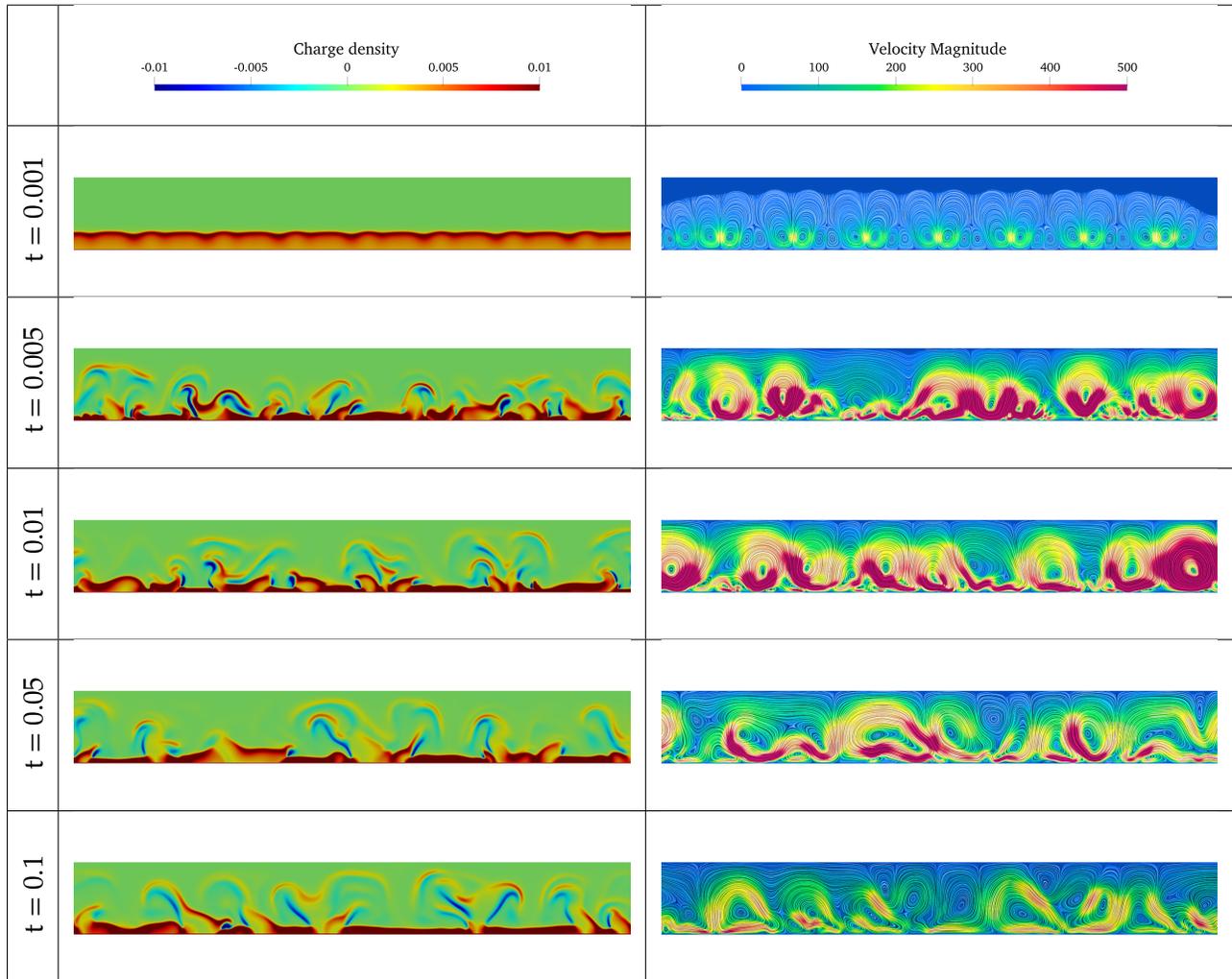
Figure 7: Contour plots of charge density and velocity magnitudes at different times for $\Delta\phi = 120$.
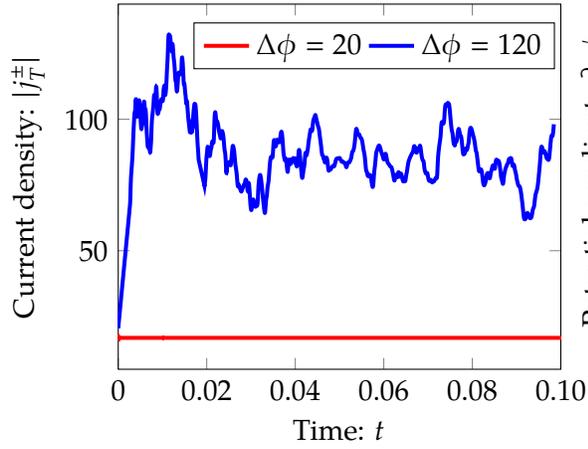
(a) Variation of current with time
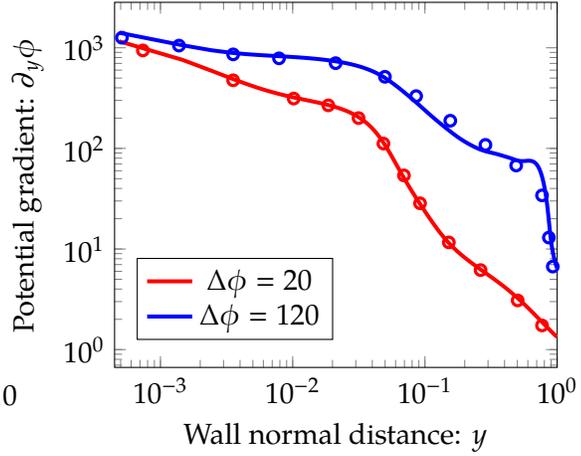
(b) Variation of potential gradient with y
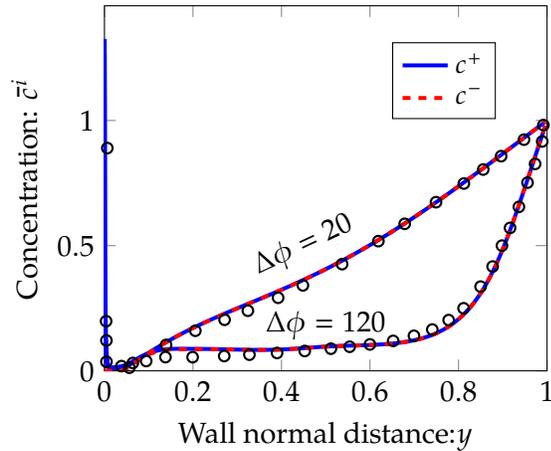
(c) Variation of concentration with y
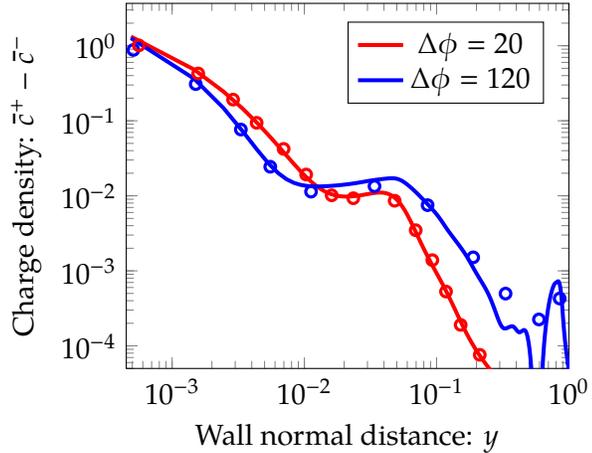
(d) Variation of charge density with y

Figure 8: *Electro-osmotic instability:* Variation of current with time (in s) for different $\Delta\phi$ is shown in Fig. 8a. Time and X averaged variation of potential gradient ($\partial_y\phi$) (Fig. 8b), concentration (Fig. 8c) and charge density (Fig. 8d) with wall normal distance y for $\Delta\phi = 20$ and 120. The dotted markers in the plot corresponds to the previous DNS results by Druzgalski et al. [16]

5.4. Packed bed ion concentration polarization: Complex geometries, small EDLs, and upstream vortex formation

Our final example illustrates a simulation of ion concentration polarization (ICP) – a phenomenon used in a wide array of electrochemical unit operations – in a realistic, state-of-art engineering device. The device consists of a packed bed of metallic beads that act as a set of electrodes embedded within a microfluidic device. This device was recently studied experimentally by Berzina et al. [62] to circumvent two challenges faced by conventional ICP occurring at a planar electrode, detailed in the next paragraph. The device configuration offers a challenging canonical simulation example due to (a) the complex geometries of the electrodes involved, (b) the steep gradients (especially near these complex geometries), and small EDL's produced by the operating conditions, (c) the ensuing channel scale vortical structures that have to be accurately resolved, and (d) the long time horizon over which the current measurements stabilize.

There has been a growing interest in ICP due to its ability to enrich and separate charged species. The key idea of ICP is to manipulate target analytes by leveraging a high electric field in the ion depletion zone (IDZ) created by selective charge transport. Previous studies have successfully demonstrated a variety of applications, including seawater desalination [8], hemodialysis [63], analyte preconcentration [64], and manipulation of neutral species following their partition in to ionic micelles [65], all using planar ICP. However, two challenges preclude the scaling up of ICP from enabling commercial deployment. First, an IDZ formed at a planar membrane or electrode may not extend across the full channel cross-section under the flow rate employed for focusing, thereby allowing the analyte to "leak" past the IDZ. Second, within the IDZ, large fluid vortices lead to mixing, which decreases the efficiency of analyte enrichment and worsens with increased channel dimensions. A promising approach has been to move away from a planar electrode (along the bottom of the channel) to using engineered, porous electrodes across the channel cross-section. Recently, Berzina et al. [62] introduced 3-D packed bed electrodes that successfully control unwanted instabilities and extend high electric field area for enrichment of bioanalytes prior to detection. In a follow-up study by Berzina et al. [66], an additional bed of packed bioconjugated beads was incorporated for DNA capture. We deploy our computational framework on this configuration to explore the impact of the packed bed electrodes on the current generation, concentration distribution, electric field extent, and vorticity patterns.

The domain consists of a cuboidal geometry with packed bed electrodes – made up of spherical beads – downstream of the channel inlet. Fluid is pushed from left to right, and a potential difference is maintained. The length, width, and height of the simulation domain are $32 \times 1 \times 1$. We only simulate a part of the width considering symmetry. On the floor of the packed bead bed, a planar electrode is located. The geometry around the packed beds is shown in Fig. 10 - Fig. 11.

A challenging aspect in such simulations is the need to construct an adaptively refined mesh of this complex geometry. Here, the octree-based adaptive meshing feature in our framework allows us to efficiently construct a high-quality mesh of the system. Fig. 9 illustrates the mesh refinement near the packed bed on a vertical plane. The refinement level ranges from 9 (bulk) to 13 (electrodes), which corresponds to the element sizes ranging from $32/2^9 \sim 0.0625$ and $32/2^{13} \sim 0.0039$, which captures physics in a wide range of length scales from the EDL around the "rough" electrode surface to the fluid flow at bulk. The non-dimensional Debye length, in this case, is 0.0036.

The details of boundary conditions are listed in Table 4. As before, the initial conditions were obtained by solving only the PNP equations until the EDL was fully developed. Then, the fully coupled NS-PNP equations were solved.

27

			Type	**Value**
NS	Sphere Top Wall Bottom Wall (no - slip)	u	Dirichlet	0
		v	Dirichlet	0
		w	Dirichlet	0
		p	Neumann	0
	Inlet	u	Dirichlet	0.371
		v	Dirichlet	0
		w	Dirichlet	0
		p	Neumann	0
	Outlet	u	Neumann	0
		v	Neumann	0
		w	Neumann	0
		p	Dirchlet	0
	Side walls		Periodic	
PNP	Sphere, Bottom electrode region (electrode)	ϕ	Dirichlet	277.1
		c_+	Dirichlet	0
		c_-	Dirichlet	0
	Inlet	ϕ	Dirichlet	0
		c^+	Dirichlet	1
		c^-	Neumann	1
	Outlet	ϕ	Neumann	0
		c^+	Neuman	0
		c^-	Neumann	0
	Bottom Wall except the electrode	ϕ	Neumann	0
		c^+	Neuman	0
		c^-	Neumann	0
	Side walls		Periodic	

Table 4: Boundary condition for 3-D electrode packed bed ICP
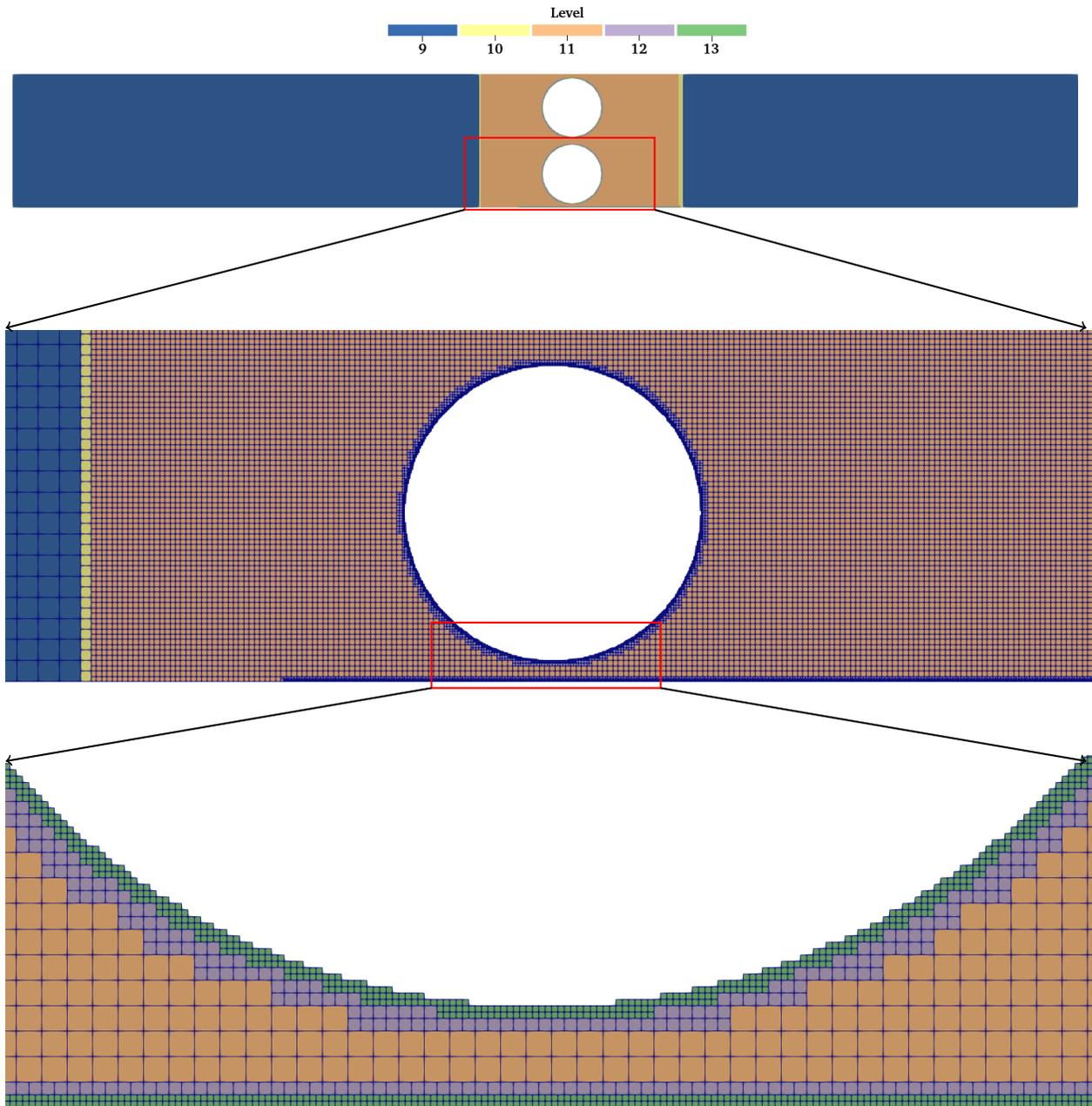
Figure 9: **Adaptive mesh refinement:** Figure showing the mesh refinement across a Z slice for the microbeads case described in Section 5.4. The overall mesh varies by 5 levels, i.e. element lengths can vary by a factor of $2^5 = 32\times$ in each direction, resulting in $> 10^4\times$ difference in the volume difference between the coarse and fine resolution.

We compare the spatial variations in the electric field, charge densities, and flow fields between two cases: a microchannel with a packed bead electrode as described above versus a microchannel with only a planar electrode. We first compare the magnitude and extent of the electric field in Fig. 10. We see that the presence of the microbeads causes the local enhancement of the electric field to extend throughout the channel cross section rather than being concentrated only in the bottom region. We note that these observations are qualitatively consistent with the ones reported in the experimental study of Berzina et al. [62].

Next, we compare the flow fields between the two cases in Fig. 11. Note the set of vortices that span the channel width, with each vortex pair nearly spanning the channel height. This is in contrast to a single large vortex in the planar electrode case. The increased region over which the electric field acts induces a larger velocity field upstream of the packed bed. However, experimental evidence suggests that this does not cause any electroconvective instabilities. The absence of electroconvective instabilities is confirmed by visualizing the ionic strength in Fig. 12.

6. Conclusions and future work

Direct numerical simulations of the coupled NS-PNP equations are challenging due to the 1) wide ranges of time and length scales exhibited by the multiscale physics, 2) chaotic flow features that often trigger numerical instabilities, and 3) geometric complexities that escalate the computational cost. In this work, we presented a finite element based numerical framework that addresses those challenges by incorporating 1) Variational multiscale pressure stabilization, 2) hybridized semi-implicit and fully implicit time integration schemes, and 3) highly parallelized adaptive meshing.

We demonstrate the utility of the framework using a series of numerical examples. The temporal and spatial convergence tests were performed to verify the order of accuracy of the numerical framework. Next, the simulation results for an electroosmotic flow were compared with its analytical solution. Then, we performed simulations capturing electrohydrodynamic instabilities near an ion-selective surface. These simulations showed excellent agreement with previously reported direct numerical simulations. Moreover, the proposed numerical scheme enabled using time steps three orders of magnitude larger than the benchmarking study, allowing significant savings in computational costs. Finally, we deployed the framework for simulating a practical microfluidics application for analyte preconcentration, which involves a complex geometry. The adaptive meshing and numerical approach are able to capture the impact of the complex geometry of 3-D electrodes. The simulation confirmed the effect of the 3-D electrodes on suppressing unwanted vortices and extending the high electric field area, and this phenomenon was also observed in the experimental work.

In summary, our proposed numerical framework addresses the challenges involved in detailed simulations of electrokinetic phenomena for practical applications. The numerical framework offers robustness for simulations with numerical instabilities, the ability to take large time steps to reach long-time horizon simulations, and adaptive octree-based meshing to resolve geometric complexities, all packaged within a massively scalable software stack.

References

[1] I. Rubinstein, B. Zaltzman, O. Kedem, Electric fields in and around ion-exchange membranes, Journal of membrane science 125 (1997) 17–21.

[2] V. Fleury, J.-N. Chazalviel, M. Rosso, Coupling of drift, diffusion, and electroconvection, in the vicinity of growing electrodeposits, Physical Review E 48 (1993) 1279.

(a)

(b)
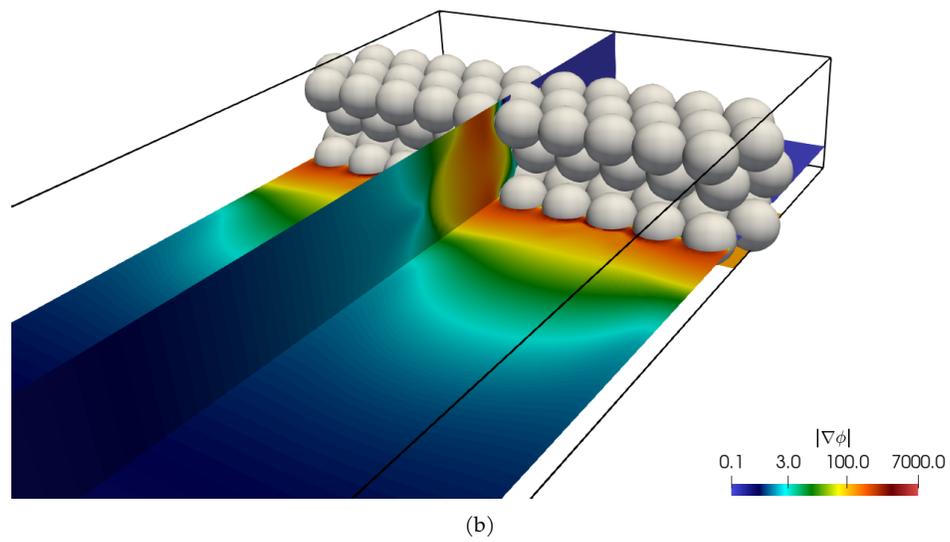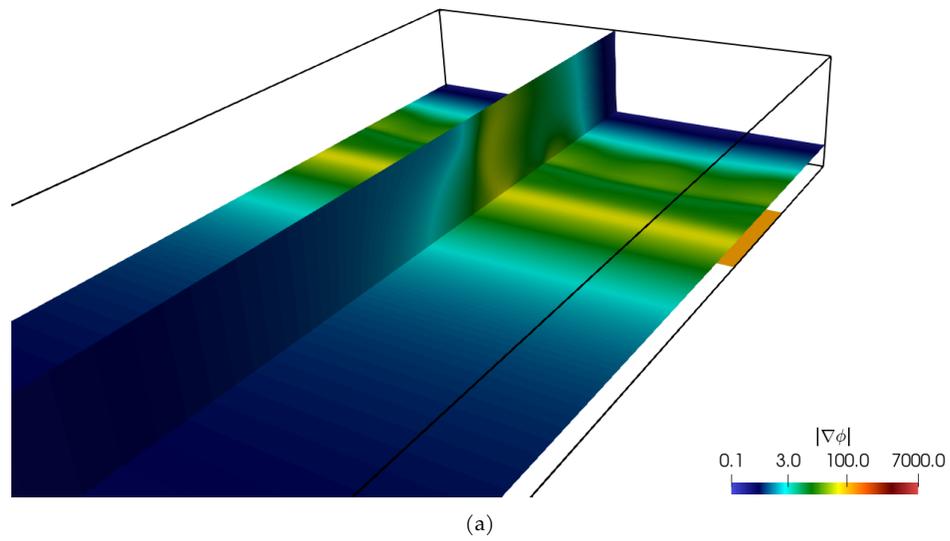
Figure 10: The magnitude of the electric field (a) only with the plate electrode, and (b) with added 3-D electrode bed.
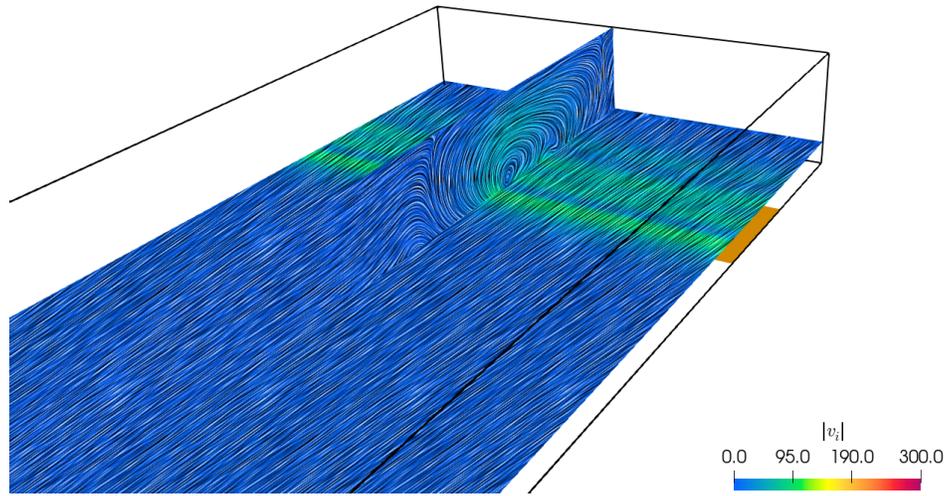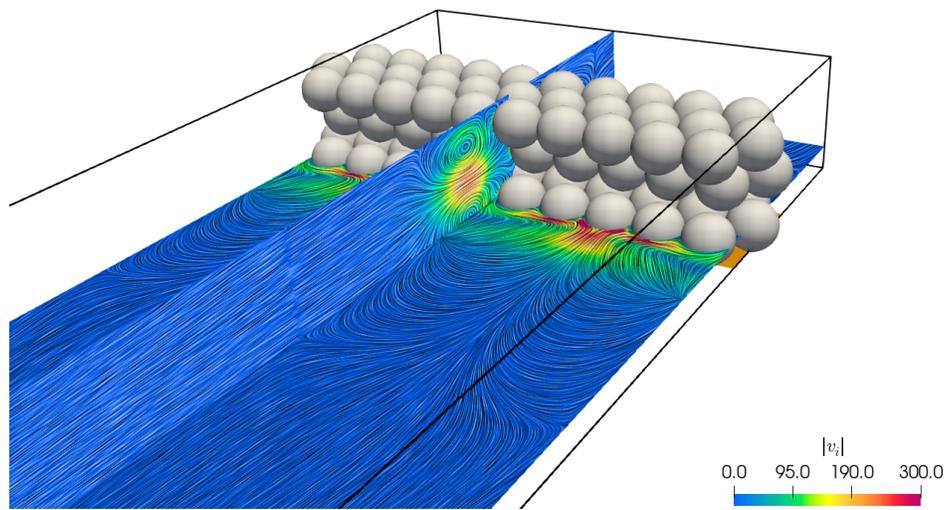
Figure 11: The flow streamline and magnitude around the electrodes. (a) only with the plate electrode, and (b) with added 3-D electrode bed.
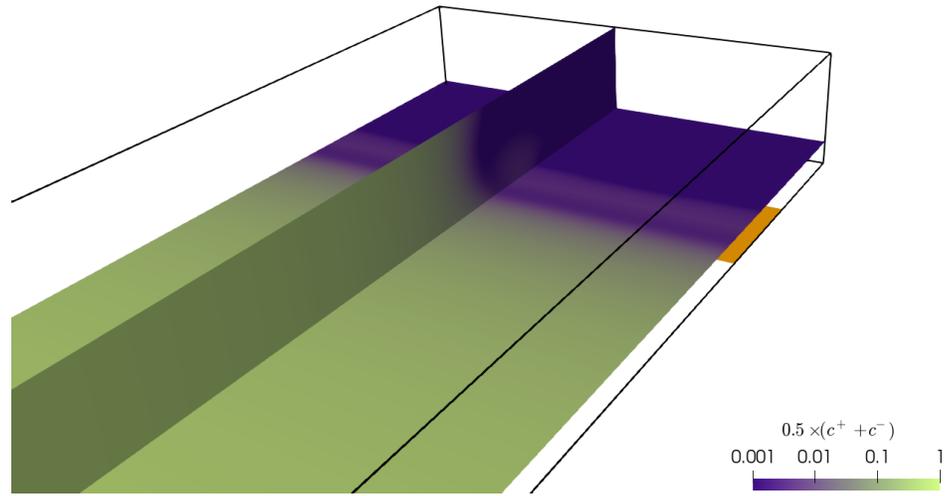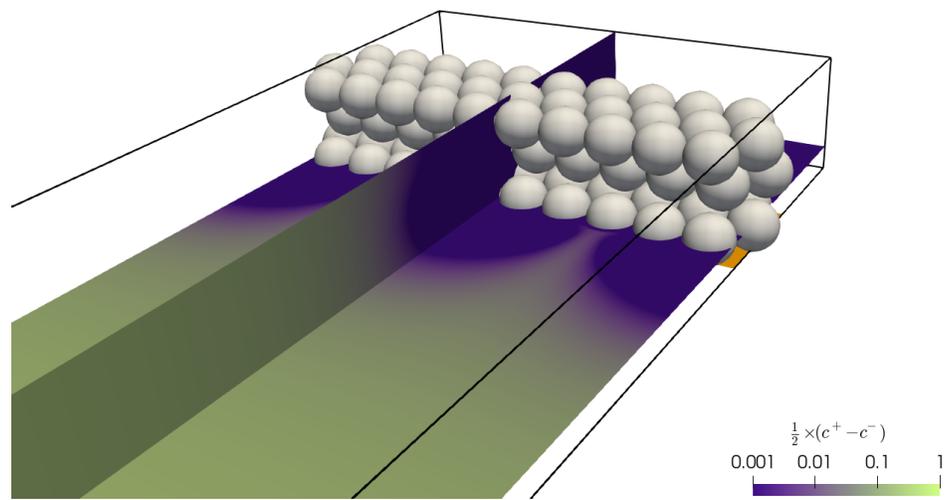
Figure 12: The ionic strength (average concentration in this case) (a) only with the plate electrode, and (b) with added 3-D electrode bed.

[3] V. Fleury, J. Kaufman, D. Hibbert, Mechanism of a morphology transition in ramified electrochemical growth, Nature 367 (1994) 435–438.

[4] J. M. Huth, H. L. Swinney, W. D. McCormick, A. Kuhn, F. Argoul, Role of convection in thin-layer electrodeposition, Physical Review E 51 (1995) 3444.

[5] R. Kwak, K. M. Lim, J. Han, et al., Shear flow of an electrically charged fluid by ion concentration polarization: Scaling laws for electroconvective vortices, Physical review letters 110 (2013) 114501.

[6] M. Wessling, L. G. Morcillo, S. Abdu, Nanometer-thick lateral polyelectrolyte micropatterns induce macrosopic electro-osmotic chaotic fluid instabilities, Scientific reports 4 (2014) 1–5.

[7] J. Chi, H. Yu, Water electrolysis based on renewable energy for hydrogen production, Chinese Journal of Catalysis 39 (2018) 390–394.

[8] S. J. Kim, S. H. Ko, K. H. Kang, J. Han, Direct seawater desalination by ion concentration polarization, Nature nanotechnology 5 (2010) 297–301.

[9] R. Kwak, V. S. Pham, B. Kim, L. Chen, J. Han, Enhanced salt removal by unipolar ion conduction in ion concentration polarization desalination, Scientific reports 6 (2016) 1–11.

[10] V. V. Nikonenko, A. V. Kovalenko, M. K. Urtenov, N. D. Pismenskaya, J. Han, P. Sistat, G. Pourcelly, Desalination at overlimiting currents: State-of-the-art and perspectives, Desalination 342 (2014) 85–106.

[11] E. W. Lees, B. A. Mowbray, F. G. Parlane, C. P. Berlinguette, Gas diffusion electrodes and membranes for co2 reduction electrolysers, Nature Reviews Materials 7 (2022) 55–64.

[12] L.-C. Weng, A. T. Bell, A. Z. Weber, Modeling gas-diffusion electrodes for co 2 reduction, Physical Chemistry Chemical Physics 20 (2018) 16973–16984.

[13] S. Kim, B. Ganapathysubramanian, R. K. Anand, Concentration enrichment, separation, and cation exchange in nanoliter-scale water-in-oil droplets, Journal of the American Chemical Society 142 (2020) 3196–3204.

[14] R. K. Anand, S. Kim, B. Ganapathysubramanian, Concentration enrichment, separation and cation exchange in water-in-oil droplets, 2022. US Patent App. 17/450,931.

[15] S. Devarakonda, S. Kim, B. Ganapathysubramanian, P. Shrotriya, Designing asymmetrically modified nanochannel sensors using virtual eis, Electrochimica Acta 403 (2022) 139694.

[16] C. Druzgalski, M. Andersen, A. Mani, Direct numerical simulation of electroconvective instability and hydrodynamic chaos near an ion-selective surface, Physics of Fluids 25 (2013) 110804.

[17] J. Kim, I. Cho, H. Lee, S. J. Kim, Ion concentration polarization by bifurcated current path, Scientific reports 7 (2017) 1–12.

[18] E. V. Dydek, B. Zaltzman, I. Rubinstein, D. Deng, A. Mani, M. Z. Bazant, Overlimiting current in a microchannel, Physical review letters 107 (2011) 118301.

[19] J.-H. Han, E. Khoo, P. Bai, M. Z. Bazant, Over-limiting current and control of dendritic growth by surface conduction in nanopores, Scientific reports 4 (2014) 1–8.

[20] S. Nam, I. Cho, J. Heo, G. Lim, M. Z. Bazant, D. J. Moon, G. Y. Sung, S. J. Kim, Experimental verification of overlimiting current by surface conduction and electro-osmotic flow in microchannels, Physical review letters 114 (2015) 114501.

[21] A. Mani, K. M. Wang, Electroconvection near electrochemical interfaces: Experiments, modeling, and computation, Annual Review of Fluid Mechanics 52 (2020) 509–529.

[22] S. M. Davidson, M. B. Andersen, A. Mani, Chaotic induced-charge electro-osmosis, Physical review letters 112 (2014) 128302.

[23] S. M. Davidson, M. Wessling, A. Mani, On the dynamical regimes of pattern-accelerated electroconvection, Scientific reports 6 (2016) 1–10.

[24] M. Jia, T. Kim, Multiphysics simulation of ion concentration polarization induced by nanoporous membranes in dual channel devices, Analytical chemistry 86 (2014) 7360–7367.

[25] L. Gong, W. Ouyang, Z. Li, J. Han, Direct numerical simulation of continuous lithium extraction from high mg2+/li+ ratio brines using microfluidic channels with ion concentration polarization, Journal of membrane science 556 (2018) 34–41.

[26] M. Seo, W. Kim, H. Lee, S. J. Kim, Non-negligible effects of reinforcing structures inside ion exchange membrane on stabilization of electroconvective vortices, Desalination 538 (2022) 115902.

[27] E. Karatay, C. L. Druzgalski, A. Mani, Simulation of chaotic electrokinetic transport: Performance of commercial software versus custom-built direct numerical simulation codes, Journal of colloid and interface science 446 (2015) 67–76.

[28] S. A. Roberts, V. E. Brunini, K. N. Long, A. M. Grillet, A framework for three-dimensional mesoscale modeling of anisotropic swelling and mechanical deformation in lithium-ion electrodes, Journal of The Electrochemical Society 161 (2014) F3052.

[29] S. A. Roberts, H. Mendoza, V. E. Brunini, B. L. Trembacki, D. R. Noble, A. M. Grillet, Insights into lithium-ion battery degradation and safety mechanisms from mesoscale simulations using experimentally reconstructed mesostructures, Journal of Electrochemical Energy Conversion and Storage 13 (2016).

[30] S. Kim, M. A. Khanwale, R. K. Anand, B. Ganapathysubramanian, Computational framework for resolving boundary layers in electrochemical systems using weak imposition of dirichlet boundary conditions, Finite Elements in Analysis and Design 205 (2022) 103749.

[31] J. Volker, Finite Element Methods for Incompressible Flow Problems, volume 51 of *Springer Series in Computational Mathematics Book*, Springer, 2016.

[32] J. Lim, J. Whitcomb, J. Boyd, J. Varghese, Transient finite element analysis of electric double layer using nernst–planck–poisson equations with a modified stern layer, Journal of Colloid and Interface Science 305 (2007) 159–174.

[33] B. Lu, M. J. Holst, J. A. McCammon, Y. Zhou, Poisson–nernst–planck equations for simulating biomolecular diffusion–reaction processes i: Finite element solutions, Journal of computational physics 229 (2010) 6979–6994.

[34] Y. Sun, P. Sun, B. Zheng, G. Lin, Error analysis of finite element method for poisson–nernst–planck equations, Journal of Computational and Applied Mathematics 301 (2016) 28–43.

[35] H. Gao, D. He, Linearized conservative finite element methods for the nernst–planck–poisson equations, Journal of Scientific Computing 72 (2017) 1269–1289.

[36] M. He, P. Sun, Mixed finite element analysis for the poisson–nernst–planck/stokes coupling, Journal of Computational and Applied Mathematics 341 (2018) 61–79.

[37] H. Liu, W. Maimaitiyiming, Efficient, positive, and energy stable schemes for multi-d poisson–nernst–planck systems, Journal of Scientific Computing 87 (2021) 1–36.

[38] H. Liu, Z. Wang, P. Yin, H. Yu, Positivity-preserving third order dg schemes for poisson–nernst–planck equations, Journal of Computational Physics 452 (2022) 110777.

[39] M. Dehghan, Z. Gharibi, R. Ruiz-Baier, Optimal error estimates of coupled and divergence-free virtual element methods for the poisson–nernst–planck/navier–stokes equations, arXiv preprint arXiv:2207.02455 (2022).

[40] Q. Chen, X. Liu, Y. Lei, H. Zhu, An electrokinetic preconcentration trapping pattern in electromembrane microfluidics, Physics of Fluids 34 (2022) 092009.

[41] H. Sundar, R. Sampath, G. Biros, Bottom-up construction and 2:1 balance refinement of linear octrees in parallel, SIAM Journal on Scientific Computing 30 (2008) 2675–2708. doi:doi:10.1137/070681727.

[42] C. Burstedde, L. C. Wilcox, O. Ghattas, p4est: Scalable algorithms for parallel adaptive mesh refinement on forests of octrees, SIAM Journal on Scientific Computing 33 (2011) 1103–1133. doi:doi:10.1137/100791634.

[43] M. Fernando, D. Neilsen, H. Lim, E. Hirschmann, H. Sundar, Massively parallel simulations of binary black hole intermediate-mass-ratio inspirals, SIAM Journal on Scientific Computing 41 (2019) C97–C138. URL: https://doi.org/10.1137/18M1196972. doi:doi:10.1137/18M1196972. arXiv:https://doi.org/10.1137/18M1196972.

[44] M. Fernando, D. Duplyakin, H. Sundar, Machine and application aware partitioning for adaptive mesh refinement applications, in: Proceedings of the 26th International Symposium on High-Performance Parallel and Distributed Computing, HPDC '17, ACM, New York, NY, USA, 2017, pp. 231–242. URL: http://doi.acm.org/10.1145/3078597.3078610. doi:doi:10.1145/3078597.3078610.

[45] M. A. Khanwale, A. D. Lofquist, H. Sundar, J. A. Rossmanith, B. Ganapathysubramanian, Simulating two-phase flows with thermodynamically consistent energy stable cahn-hilliard navier-stokes equations on parallel adaptive octree based meshes, Journal of Computational Physics 419 (2020) 109674.

[46] M. A. Khanwale, K. Saurabh, M. Fernando, V. M. Calo, J. A. Rossmanith, H. Sundar, B. Ganapathysubramanian, A fully-coupled framework for solving cahn-hilliard navier-stokes equations: Second-order, energy-stable numerical methods on adaptive octree based meshes, arXiv preprint arXiv:2009.06628 (2020).

[47] K. Saurabh, B. Gao, M. Fernando, S. Xu, M. A. Khanwale, B. Khara, M.-C. Hsu, A. Krishnamurthy, H. Sundar, B. Ganapathysubramanian, Industrial scale large eddy simulations with adaptive octree meshes using immersogeometric analysis, Computers & Mathematics with Applications 97 (2021) 28–44.

[48] S. Xu, B. Gao, A. Lofquist, M. Fernando, M.-C. Hsu, H. Sundar, B. Ganapathysubramanian, An octree-based immersogeometric approach for modeling inertial migration of particles in channels, Computers & Fluids 214 (2021) 104764.

[49] B. Kirby, Micro- and Nanoscale Fluid Mechanics: Transport in Microfluidic Devices, Cambridge University Press, 2010. URL: https://books.google.com/books?id=y7PB9f5zmU4C.

[50] C. L. Druzgalski, M. B. Andersen, A. Mani, Direct numerical simulation of electroconvective instability and hydrodynamic chaos near an ion-selective surface, Physics of Fluids 25 (2013) 110804–110804. doi:doi:10.1063/1.4818995.

[51] T. Tezduyar, S. Mittal, S. Ray, R. Shih, Incompressible flow computations with stabilized bilinear and linear equal-order-interpolation velocity-pressure elements, Computer Methods in Applied Mechanics and Engineering 95 (1992) 221–242.

[52] T. J. Hughes, G. Scovazzi, L. P. Franca, Multiscale and stabilized methods, Encyclopedia of Computational Mechanics Second Edition (2018) 1–64.

[53] T. J. Hughes, Multiscale phenomena: Green's functions, the Dirichlet-to-Neumann formulation, subgrid scale models, bubbles and the origins of stabilized methods, Computer Methods in Applied Mechanics and Engineering 127 (1995) 387–401.

[54] Y. Bazilevs, V. Calo, J. Cottrell, T. Hughes, A. Reali, G. Scovazzi, Variational multiscale residual-based turbulence modeling for large eddy simulation of incompressible flows, Computer Methods in Applied Mechanics and Engineering 197 (2007) 173–201.

[55] T. J. Hughes, L. Mazzei, K. E. Jansen, Large eddy simulation and the variational multiscale method, Computing and Visualization in Science 3 (2000) 47–59.

[56] W. Zhang, A. Almgren, V. Beckner, J. Bell, J. Blaschke, C. Chan, M. Day, B. Friesen, K. Gott, D. Graves, et al., Amrex: a framework for block-structured adaptive mesh refinement, Journal of Open Source Software 4 (2019) 1370–1370.

[57] S. Popinet, Gerris: a tree-based adaptive solver for the incompressible euler equations in complex geometries, Journal of computational physics 190 (2003) 572–600.

[58] K. Saurabh, M. Ishii, M. Fernando, B. Gao, K. Tan, M.-C. Hsu, A. Krishnamurthy, H. Sundar, B. Ganapathysubramanian, Scalable adaptive pde solvers in arbitrary domains, in: Proceedings of the International Conference for High Performance Computing, Networking, Storage and Analysis, 2021, pp. 1–15.

[59] K. Saurabh, M. Ishii, M. A. Khanwale, H. Sundar, B. Ganapathysubramanian, Scalable adaptive algorithms for next-generation multiphase simulations, arXiv preprint arXiv:2209.12130 (2022).

[60] M. Ishii, M. Fernando, K. Saurabh, B. Khara, B. Ganapathysubramanian, H. Sundar, Solving pdes in space-time: 4d tree-based adaptivity, mesh-free and matrix-free approaches, in: Proceedings of the International Conference for High Performance Computing, Networking, Storage and Analysis, 2019, pp. 1–61.

[61] M. A. Khanwale, K. Saurabh, M. Ishii, H. Sundar, J. A. Rossmanith, et al., A projection-based, semi-implicit time-stepping approach for the cahn-hilliard navier-stokes equations on adaptive octree meshes, arXiv preprint arXiv:2107.05123 (2021).

[62] B. Berzina, S. Kim, U. Peramune, K. Saurabh, B. Ganapathysubramanian, R. K. Anand, Out-of-plane faradaic ion concentration polarization: stable focusing of charged analytes at a three-dimensional porous electrode, Lab on a Chip (2022).

[63] B. Berzina, R. K. Anand, An electrokinetic separation route to source dialysate from excess fluid in blood, Analytical chemistry 90 (2018) 3720–3726.

[64] S. H. Ko, Y.-A. Song, S. J. Kim, M. Kim, J. Han, K. H. Kang, Nanofluidic preconcentration device in a straight microchannel using ion concentration polarization, Lab on a Chip 12 (2012) 4472–4482.

[65] B. Berzina, R. K. Anand, Continuous micellar electrokinetic focusing of neutral species driven by ion concentration polarization, Lab on a Chip 19 (2019) 2233–2240.

[66] B. Berzina, U. Peramune, E. L. Claus, S. Kim, K. Saurabh, M. E. Strait, B. Ganapathysubramanian, R. Anand, Electrokinetic enrichment and label-free electrochemical detection of nucleic acids by conduction of ions along the surface of bioconjugated beads for point-of-care testing (2022).